RECEIVED BY TIC JUN 17 1980

LBL-10039

Lawrence Berkeley Laboratory
UNIVERSITY OF CALIFORNIA

Physics, Computer Science & Mathematics Division

LIMITED-ANGLE IMAGING IN POSITRON CAMERAS: THEORY AND PRACTICE

MASTER

Kwok Cheong Tam
(Ph.D. thesis)

October 1979

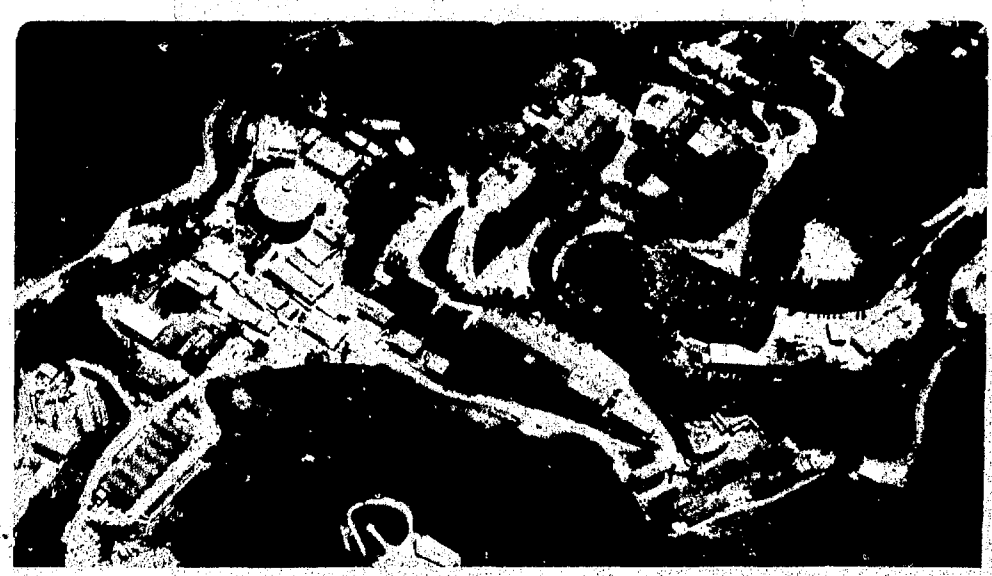

Prepared for the U.S. Department of Energy under Contract W-7405-ENG-48

DISTRIBUTION OF THIS DOCUMENT IS UNLIMITED

LIMITED-ANGLE IMAGING IN POSITRON CAMERA--THEORY AND PRACTICE

Contents

ABSTRACT vii

ACKNOWLEDGMENTS ix

I. INTRODUCTION 1

II. THEORY OF POSITRON IMAGING 7

2.1. Detection of Annihilation Gammas 8

2.1.1. Multiwire Proportional Chamber 8

2.1.2. Delay Line Readout 5

2.1.3. Gamma Converter 15

2.1.3.1. Conversion Efficiency. 17

2.1.3.2. Extraction Efficiency. 23

2.1.4. Event Rate Consideration 26

2.1.4.1. Singles Rate 30

2.1.4.2. True Coincidence Rate. 30

2.1.4.3. Chance Coincidence Rate. 32

2.1.4.4. Ratio of True to Chance Coincidences 33

2.2. 3-D Reconstruction in Positron Camera. 36

2.2.1. Solving the Integral Equation. 36

2.2.2. The Optical Transfer Function and the Undetermined Frequency Components. . . 43

2.2.3. Use of a Priori Information 50

2.2.3.1. Finite Spacing 51

2.2.3.2. Finite Extent of Object. 51

DISCLAIMER

III. DATA TREATMENTS AND ERROR ANALYSIS. 63

3.1. Compton Scattering. 63

3.1.1. Delay Line Sum Pulse Rejection. 63

3.1.2. Digital Filtering 70

3.2. Error Propagation and Stabilization in Reconstructions 75

3.2.1. Deconvolution Followed by Iterations. 75

3.2.2. Matrix Inversion. 84

3.2.3. Comparison Between Deconvolution + Iterations and Matrix Inversion 89

IV. IMPLEMENTATION 92

4.1. MWPC-Gamma Converter Positron Camera System 92

4.1.1. The Detection Assembly. 95

4.1.2. The Electronics System. 99

4.2. Reconstruction Results 103

4.2.1. Computer-Simulated Data 104

4.2.2. Real Data 121

V. DISCUSSIONS AND CONCLUSIONS 128

5.1. Discussions 128

5.2. Conclusions 131

APPENDIX A Evaluation of $I = \int_0^{t/2} (L + 2x)P_{esc}(x,E_i)dx$. 132

APPENDIX B Track-Length Distribution Inside an Infinitely Long Cylinder with Source Point Outside the Cylinder . . 135

APPENDIX C Derivation of the Factor $C(T_r/T_c)$ in the True Coincidence Rate When $T_r \leq T_c$. 139

APPENDIX D Evaluation of the Two-Dimensional Optical Transfer Function 143

APPENDIX E Evaluation of the Three-Dimensional Optical Transfer Function 144

APPENDIX F Necessary and Sufficient Condition for an Optical Transfer Function to be Non-Zero Everywhere . . . 145

APPENDIX G Effects of Sampling ϕ_0 (x, z) in the x and z Dimensions 147

APPENDIX H Proof for the Positive Definiteness of BA 149

APPENDIX I Lower Bound of the Eigenvalues of the Matrix Integral Operator 150

REFERENCES 152

LIMITED-ANGLE IMAGING IN POSITRON CAMERA--THEORY AND PRACTICE

Kwok-Cheong Tam

Computer Science and Applied Mathematics Department
Lawrence Berkeley Laboratory, University of California
Berkeley, California 94720

ABSTRACT

The principles of operation of planar positron camera systems made up of multiwire proportional chambers as detectors and electromagnetic delay lines for coordinate readout are discussed. Gamma converters are coupled to the wire chambers to increase detection efficiency and improve spatial resolution. The conversion efficiencies of these converters are calculated and the results compare favorably to the experimentally measured values.

Two reconstruction algorithms, Fourier deconvolution and matrix inversion, for obtaining the three-dimensional distribution of the radioisotopes from the recorded data are described. Construction of generalized tomograms capable of emphasizing the large-angle events is introduced. The effects of the angular range of data taking in reconstructions using the two algorithms are investigated. It is found that in the absence of any a priori information there are undetermined components in the reconstruction if the point response function of the positron camera does not satisfy certain criteria. However, most of the undetermined components are recovered in the case in which the transverse spacing of the object is discrete, and all of them are

recovered if the fact that the object extent is finite is utilized. An iterative scheme for recovering these undetermined components is developed, which is applicable to other transmission and emission imaging devices.

Experimental and digital methods for suppressing the noise in the data due to Compton scattering are detailed. The propagation of errors in the reconstruction algorithms is formulated, and methods to stabilize their performance in the presence of noise are developed.

Results of reconstructing a real phantom as well as computer-generated phantoms are presented.

ACKNOWLEDGMENTS

This work was supported financially by the Physics Division of the Department of Energy under contract No. W-7405-ENG-48 and by the National Institute of Health.

I like to thank Dr. Victor Perez-Mendez for supervising the progress of this project and giving helpful advice. I am greatly indebted to Dr. Gilbert Chu, who initiated the deconvolution reconstruction algorithm, and Drs. Chun Bun Lim and Dennis Chu, who constructed the positron camera. In addition, their constructive suggestions and support are vital to the success of this work. I also wish to extend my appreciation to Dr. Alberto Grunbaum and Dr. Burns Macdonald for their interest and fruitful discussions.

A special note of gratitude goes to Miss Brenda Tang for her moral support and encouragement while much of this work was being done, and for her help in preparing the draft.

Finally, to God, who provided me with this research opportunity and enabled me to accomplish it, my thanks are due.

I. INTRODUCTION

The past decade has seen a rapid development in the field of nuclear medicine, the use of radioisotope tracers for diagnosing medical disorders. Such rapid progress is attributed to the availability of many new radiopharmaceuticals on one hand, and the improvement of radioisotope imaging devices and image reconstruction methods on the other. The general procedure is to administer a gamma-emitting radioisotope with appropriate half-life to a patient. The gamma radiation which escapes from the patient's body is detected by a gamma detector, and the data so accumulated are processed to give an estimate of the distribution or localization of the radioisotope, which is a reflection of the condition of the organ under diagnosis.

An imaging system in nuclear medicine is made up of three basic components: (1) the gamma-ray channel, which selects and directs the gamma radiation from the object to the detector; (2) the detector, which is sensitive to the gamma radiation; (3) the data processor, which processes the data acquired by the detector to produce an image of the radioisotope distribution. Depending on whether the detector is in motion or stationary while taking data, and the method of channeling the gamma rays, nuclear medicine imaging device can be classified into two categories: scanners, and gamma cameras.

Single-head scanners [1] were the earliest devices employed in radioisotope imaging: a detector equipped with a collimator scans rectilinearly over the area of interest (Fig. I.1). At any instant of

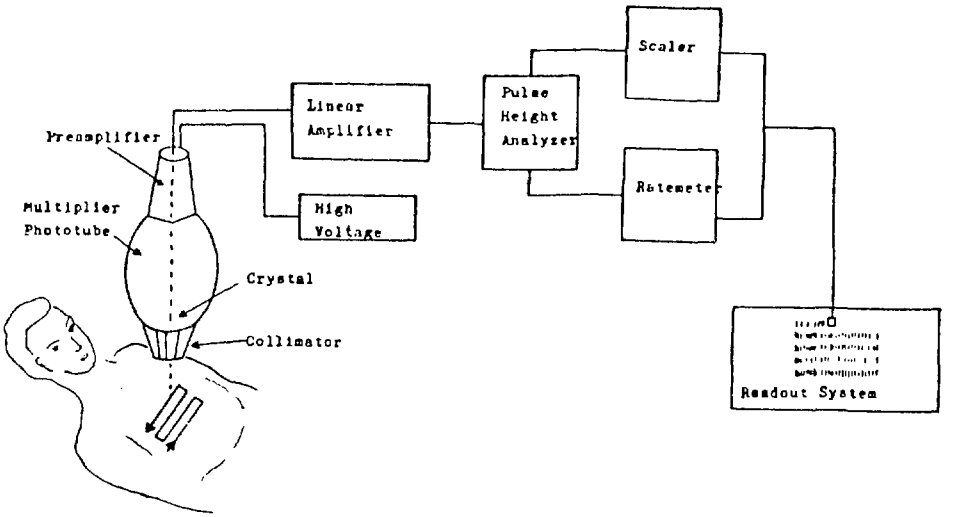

Fig. 1.1. Schematic configuration of a scanner.

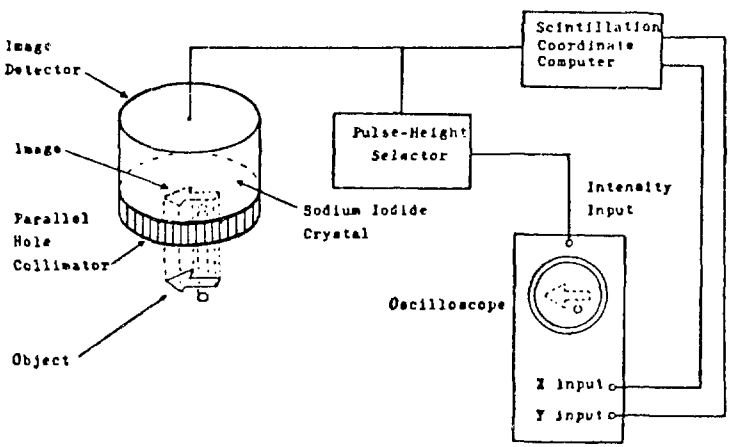

XBL 796-10294

Fig. 1.2. Schematic configuration of a Gamma camera.

data acquisition the collimator, either in the form of a single cylindrical bore, or a cluster of tapered apertures focused at a fixed point, allows the gamma rays from a single resolution element to fall on the detector while blocking out those from the rest of the organ. Recording the detector signal as a function of the scanning position permits a two-dimensional distribution of the gamma-emitting radioisotope to be mapped out. In recent years multi-head rectilinear scanners [2] have been developed and increasingly used for organ scanning, especially for the larger ones such as lung and liver/spleen, and whole body scanning. Their design is fundamentally the same as that of single-head scanners, except that instead of a single scan, two or more scans are obtained from different directions.

In constrast to the scanners, gamma cameras are, in general, stationary devices, though recently some moving cameras are being developed [3]. Through image-producing collimators such as pinhole aperture or multi-channel collimator, their gamma detectors continuously receive radiation emitted from all parts of the object being diagnosed (Fig. 1.2). By recording the interaction sites of the incident gamma rays with the detector, an image of the radioisotope distribution can be obtained. There are a number of position-sensitive instruments which can be used as detectors in gamma cameras: the commercially available Anger camera [4] employs NaI(Tl) crystal viewed by a number of photomultiplier tubes (PMT) around its circumference; spatial resolution is achieved through pulse height division method. Other detectors such as image intensifier [5], spark chamber [6], multiwire proportional chamber [7],

and semiconductor detector [8] have also been used in experimental gamma-ray cameras.

The main advantage of these relatively new imaging devices, the gamma cameras, over the radioisotope scanners is their much faster rate of data acquisition. The reasons are two-fold. Firstly, the gamma-ray cameras collect data in parallel, the radiation from all parts of the object is detected at the same time, resulting in much higher sensitivity than is possible with the scanners which gather data sequentially. Secondly, data acquisition time is not limited by any mechanical motion, which is a determining factor in the case of scanners. The shorter exposure time of the cameras permits the recording of dynamic processes, such as blood flow and heart beat, as well as static distribution, whereas the scanners are restricted to the latter only. However, gamma-ray cameras are limited in their field of view, whereas the scanners are not so restricted. The problems imposed by the limited field of view will be discussed in detail in the next chapter.

One major source of errors in the data taken by the scanners and the cameras is the attenuation of the gamma rays by the quantity of tissue lying between the gamma-ray source and the detector. The amount of attenuation depends on the position of the gamma-ray source, and it is this position dependence which greatly complicates the image reconstruction problem. Furthermore, the septa of the collimators which provide for resolution in gamma scanners and cameras absorb a large fraction of the photons, limiting the imaging efficiency.

The use of positron-emitting radionuclides allows compensation for gamma-ray absorption and eliminates the need of collimators. Some proton-rich elements decay by emitting a positron and a neutrino to achieve stability. The positron produced will annihilate with an electron in the neighborhood, producing two back-to-back gamma rays. The direction and location of these annihilation gamma-ray pairs can be found by detecting them in coincidence without the need of a collimator; therefore positron imaging is capable of much higher sensitivity than that of gamma camera, resulting in lower dose to the patient. Moreover, the resolution is improved, as it is no longer limited by the collimator. Operation in coincidence also results in lower background count rate, and thus improves counting statistics. As for the absorption of the gamma rays, the sum of the distance traversed by the two annihilation gamma rays is roughly constant for a given patient thickness, so the attenuation is more or less independent of the location of the source.

More quantitatively, we assume that the two photons must travel distances x_1 and x_2, respectively, in the object while the distance $d = x_1+x_2$ is a slowly varying function of the annihilation point. Suppose that the effective Compton scattering attenuation coefficient for the object is given by a fixed number μ. Then the probability that both of the photons will not undergo Compton scattering is

$$P_1P_2 = \exp(-\mu x_1)\exp(-\mu x_2) = \exp(-\mu d)$$

approximately independent of the position of the annihilation point. The probability that either photon undergoes Compton scattering is therefore proportional to $1-\exp(-\mu d)$, also approximately independent of position.

One more advantage of positron imaging is that about one half of all the radionuclides are positron emitters, such as C^{11}, N^{13}, O^{15}, F^{18}, Ga^{68}, Cu^{64}, and Ru^{82}, etc. These biologically important radionuclides have short half-lives and high specific activity, thus it should theoretically be possible to find a positron emitter for almost any imaging problem of interest.

A positron imaging scanner utilizing the time-of-flight principle was introduced by Burnham et al., in 1967 [9]. Positron cameras using arrays of NaI crystals were constructed by Anger in 1967 [10]. There are also positron cameras using two large NaI crystals [11], using multiwire proportional chambers with liquid Xe [12]. The purpose of this thesis is to investigate the problems involved in imaging in positron cameras using multiwire proportional chambers equipped with gamma ray converters [13].

II. THEORY OF POSITRON IMAGING

In typical positron camera imaging, a β^+ active radioisotope is injected into the patient's blood stream in a carrier which is chosen to be preferentially absorbed by the medical anomaly. The radioisotope assumes a quasi-equilibrium distribution in the tissue. In undergoing β^+ decay, the nuclei of the radioisotope emit low energy positrons

$$p \rightarrow n + e^+ + \nu$$

about 98% of which are rapidly thermalized [14] within a short distance from their point of origin (a 1 MeV e^+ has an linear range of 5 mm in tissue). The thermalized positron then combines with a valence electron of some atom in the immediate vacinity to form a positronium, usually in the singlet state; only about 1/3 of 1% of these positroniums are formed in the triplet state, which emit three photons in the subsequent annihilations [15]. Those positroniums in the singlet state annihilate with the production of 2 gammas. By the conservation of energy and momentum, these singlet photons have an energy of approximately 511 keV, and travel very nearly in opposite directions, i.e., back to back. As the momentum of the center of mass of the annihilating pair is of the order $\sim m_0 c/137$, the 2 gammas are collinear to ~1/137 radian [16]. These annihilation gammas may subsequently escape from the patient's body and be detected by the positron camera in coincidence, with their positions of interaction with the camera recorded.

The data in a positron camera are therefore in the form of straight lines defined by the annihilation gamma pairs, with the positions

of the radioactive nuclei which have undergone β^+ decay lying somewhere along the lines. The positions of the decays can in principle be determined by the time-of-flight method, but this requires extremely high speed electronics. An alternate way is to inverse the distribution of the annihilation gamma pairs to yield the radioisotope distribution.

Thus the problem of imaging in a positron camera consists of two parts: (1) to detect the annihilation photons efficiently and record their positions accurately, and (2) to reconstruct the distribution of the radioisotope mathematically from the recorded data.

2.1. Detection of Annihilation Gammas

The requirements on the detector in positron camera are high efficiency for stopping the 511 keV photons, and good spatial resolution to define their positions of interaction. Multiwire proportional chamber (MWPC) equipped with gamma converter is a suitable combination for such purposes, besides offering large detection area at relatively low cost.

2.1.1. Multiwire Proportional Chamber

The advent of MWPC marked a great step forward in the field of particle studies. Since its development by Charpak and colleagues in 1968 [17] much work has been done in investigating the properties of the MWPC and in developing various auxiliary devices which greatly extend its scope of application. The use of MWPC in nuclear medicine imaging was first developed at Lawrence Berkeley Laboratory by Perez-Mendez and colleagues [18].

MWPC can be considered as an improved version of proportional chamber. In a MWPC, a plane grid of equally spaced wires lying between and parallel to a pair of plane cathode electrodes takes the place of the anode wire in the proportional chamber. It is equivalent to a series of quasi-independent single-wire chambers side by side, operating in the region of proportionality. The two cathode planes are made up of two planes of parallel wires orthogonal to each other.

The electric potential and field distribution in a MWPC have been calculated by Erskine [19]. For a chamber with geometric configuration as shown in Fig. 2.1, the electric potential and the electric field are given by:

$$V(x,y) \approx q\left\{\frac{2\pi L}{s} - \ln\left[4\sin^2(\pi x/s) + 4\sinh^2(\pi y/s)\right]\right\}$$

$$E_x(x,y) = -\frac{\partial V}{\partial x} = \frac{\pi q \sin(2\pi x/s)}{s\left[\sin^2(\pi x/s) + \sinh^2(\pi y/s)\right]}$$

$$E_y(x,y) = -\frac{\partial V}{\partial y} = \frac{\pi q \sinh(2\pi y/s)}{s\left[\sin^2(\pi x/s) + \sinh^2(\pi y/s)\right]}$$

where L is the plane spacing, s is the anode-wire spacing, and q is the charge per unit length on an anode wire. Figure 2.2 shows the general shape of the field lines and the equipotentials for such a geometry. At regions close to the anode wires ($x \ll s$, $y \ll s$), the electric field varies as $1/r$. The field near the wires is strong enough to enable electrons in that region to acquire sufficient energy between collisions to ionize gas molecules with which they collide.

When an ionizing particle passes through a MWPC, it liberates electrons from the gas molecules in the chamber through photoelectric

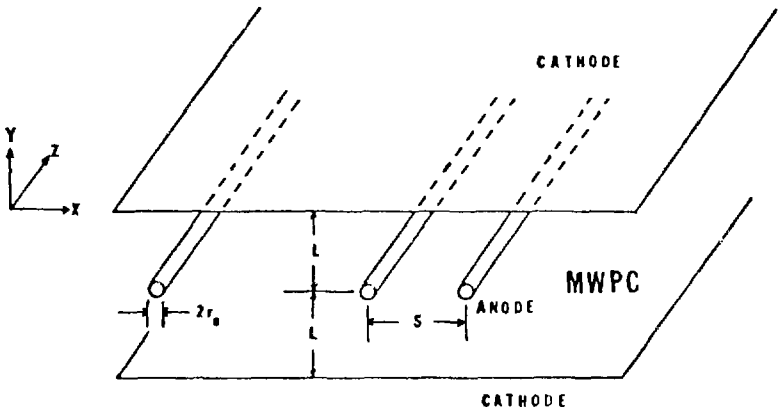

XBL 796-10296

Fig. 2.1. Graphic definition of MWPC geometric parameters.

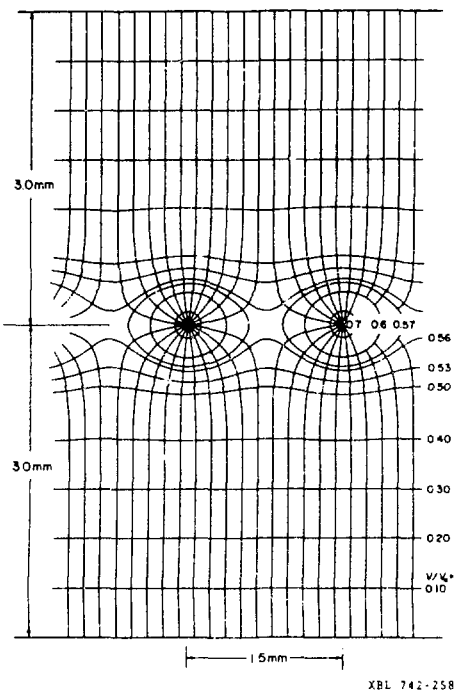

Fig. 2.2. Equipotentials and electric field lines in MWPC.

interaction or Compton scattering. The electrons produced drift toward the anode wire. As soon as they enter the multiplication region they produce secondary electrons by collisions which, in turn, produce more electrons by the same process. Consequently there form an avalanche of electrons which is collected by the anode wire, and a positive-ion sheath which moves toward the cathodes. Detailed consideration shows that the total number of electrons produced n (which is also the total number of positive ions) is proportional to the number of initial electrons n_0,

$$n = An_0.$$

The proportionality factor A is called the multiplication factor which was found by Rose and Korff [20] to be of the form

$$A = \exp 2(aNCr_0V)^{1/2} [(\frac{V}{V_s})^{1/2}-1]$$

where V is the applied potential, V_s is the threshold potential (the potential at which inelastic collisions start at the surface of the wire), r_0 is the wire radius, N is the number of gas atoms per cc, a is the rate of increase of the ionization cross section with energy, and C is the chamber capacitance per unit length.

The motion of the electrons and the positive ions induces a negative voltage pulse at the avalanche anode and a positive one at the cathodes, with the major contribution to these voltage pulses coming from the positive ion drift. These signal pulses are readout by the delay line method to be described in the next section.

2.1.2. Delay Line Readout

The use of distributed LC electromagnetic delay line furnishes a suitable way of accomplishing position-to-time conversion. The signals generated on each of the two perpendicular cathode wires are capactive-coupled to a delay line. The time differences between the time of arrival of the prompt anode signal and the delayed signals from the two cathodes give the x and y coordinates of the interaction site. A distinct advantage of this readout method is the inherent ability to interpolate between signal-coupling points for the position of the centroid of the signal. The centroid of a single pulse indicates closely the center of an ionization event even though the signal includes contribution from the adjacent wires.

In its simplest form the delay line is essentially a transmission line with uniformly distributed inductance and capacitance L and C respectively. For an ideal transmission line,

$$\frac{\partial V}{\partial z} = - L \frac{\partial I}{\partial t},$$

$$\frac{\partial I}{\partial z} = - C \frac{\partial V}{\partial t}.$$

Combining these two equations we get the wave equations,

$$\frac{\partial^2 V}{\partial z^2} = LC \frac{\partial^2 V}{\partial t^2}$$

$$\frac{\partial^2 I}{\partial z^2} = LC \frac{\partial^2 I}{\partial t^2}$$

which have the general solutions [21]

$$V(z,t) = F_1(z-v_0 t) + F_2(z+v_0 t)$$

$$Z_0 I(z,t) = F_1(z-v_0 t) - F_2(z+v_0 t)$$

the coefficients a_i being determined from the known values of $R(\underline{k})$ in the allowed cone.

Besides the prolate spheroidal functions, Fourier series can also be used in expanding the function to fill in the missing cone. This method was employed by Harris [31] to continue a one-dimensional spectrum, and by Inouye [37] to reconstruct a two-dimensional image.

A rather obvious way to extend the known portion of the spectrum $R(\underline{k})$ to the missing cone is by means of the iterative scheme shown in Fig. 2.21. The spectrum $S^{(0)}(\underline{k})$ obtained from deconvolution, with the undetermined components set to zero, is Fourier transformed to the object space. There the values outside the known extent of the object are set to zero, and then inverse transformed to the frequency space, giving $R^{(1)}(\underline{k})$. The components of $R^{(1)}(\underline{k})$ inside the allowed cone are reset to the original values given by $S^{(0)}(\underline{k})$, and the cycle repeats yielding $R^{(n)}(\underline{k})$ after n iterations.

We note that this iterative scheme has been used by Gerchberg [38] and Papoulis [39] to improve the resolution of one-dimensional signals in band-limited systems. The convergence of the scheme in one dimension has been proved by both of these authors. The proof given in Gerchberg's paper made use of the property that a real analytic function in one-dimensional space either vanishes everywhere or only has isolated zeros. This proof can be generalized to higher dimensions by using the more general property that real analytic functions on n-dimensional space cannot vanish on an infinite set of n-1 dimensional planes through the origin without vanishing identically.

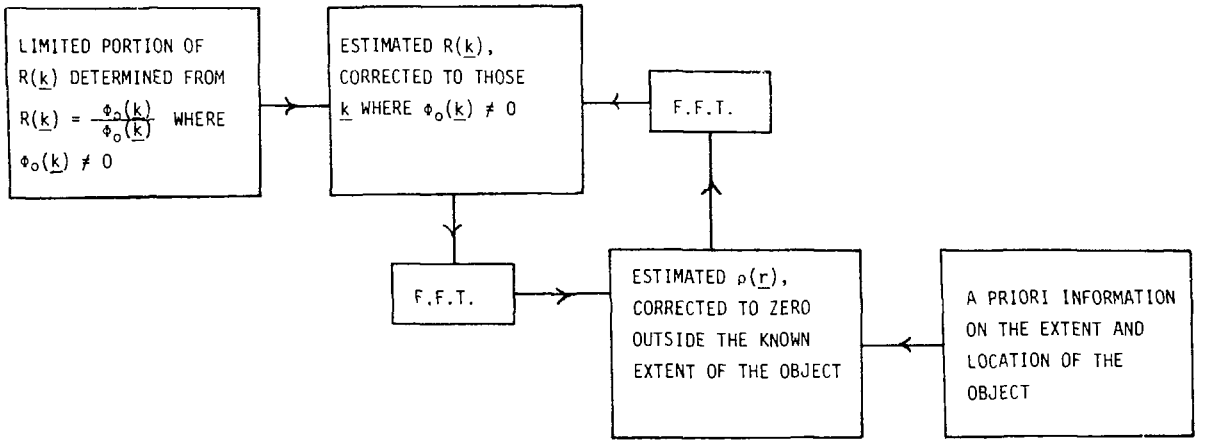

Fig. 2.21. Iterative scheme to extend the spectrum R(k) beyond the allowed cone.

XBL 796-10266

A more quantitative proof of the convergence of the iterative scheme is now given. In actual reconstruction, we will be dealing with frequency components below a certain maximum frequency determined by such factors as the spatial resolution of the imaging system, the available computer core memory, etc. In Fig. 2.22, R_a represents the region in frequency space where $R(\underline{k})$ is known, and R_b is the extent of the object. Define the operators A and B operating on functions f defined in frequency space as follows:

$$A\ f = \chi_A\ f$$
$$B\ f = F^{-1} \chi_B\ F\ f$$

where F and F^{-1} represent Fourier transformation and its inverse, and χ_A, χ_B are respectively the characteristic functions of R_a and R_b, defined as:

$$\chi_A(\underline{k}) = \begin{cases} 1 & \underline{k} \in R_a \\ 0 & \underline{k} \notin R_a \end{cases}$$

$$\chi_B(\underline{x}) = \begin{cases} 1 & \underline{x} \in R_b \\ 0 & \underline{x} \notin R_b \end{cases}.$$

With these operators we can formulate the iteration procedure as follows. If $R(\underline{k})$ represents the Fourier spectrum of the object $\rho(\underline{r})$, and $S^{(0)}(\underline{k})$ the Fourier spectrum of $\rho(\underline{r})$ obtained from deconvolution, then

$$S^{(0)}(\underline{k}) = A\ R(\underline{k}).$$

Fourier transforming $S^{(0)}(\underline{k})$ to the object space, setting the values outside the known extent of the object to zero, and then inverse transforming to the frequency space, we get the first iterated spectrum $R^{(1)}(\underline{k})$:

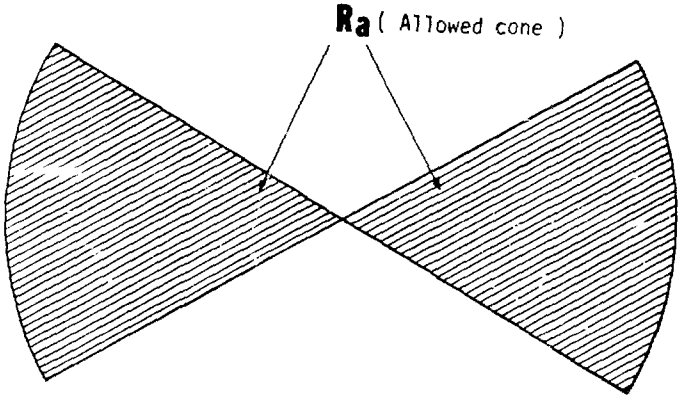

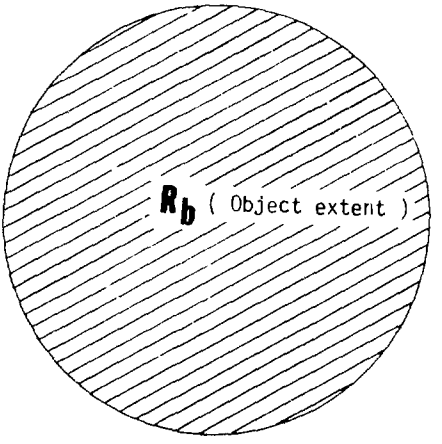

XBL 798-11176

Fig. 2.22. Schematic representations of the allowed cone and the object extent.

In Appendix II it is shown that the operator BA operating on the functions satisfying equation (2.15) is a positive definite operator. Thus the set of eigenfunctions $\{\psi_i\}$ of BA forms a complete set of functions which are orthonormal in the entire k-space, and orthogonal in the region R_a[40],

$$\int_{\text{k-space}} \psi_i(\underline{k})\, \psi_j^*(\underline{k}) d^3k = \delta_{ij}$$

$$\int_{R_a} \psi_i(\underline{k})\, \psi_j^*(\underline{k})\, d^3k = \lambda_i \delta_{ij}.$$

Thus any function f in k-space which satisfies (2.15) can be expanded in a series of ψ_i which converges to f everywhere; if $Bf \neq f$, the expansion is still valid in the region R_a, but it does not necessarily converge outside R_a. All the eigenvalues of BA lie between 0 and 1, i.e., $0 < \lambda_i < 1$.

Decompose $R(\underline{k})$ into a linear combination of ψ_i

$$R(\underline{k}) = \sum_{i=0}^{\infty} a_i \psi_i(\underline{k}).$$

Then equation (2.14) becomes

$$R^{(n)}(\underline{k}) = \sum_{i=0}^{\infty} a_i (1-(1-\lambda_i)^n) \psi_i(\underline{k}).$$

The truncation error in terminating the iteration after n steps is thus given by

$$E_t^{(n)}(\underline{k}) = R^{(n)}(\underline{k}) - R(\underline{k})$$

$$= -\sum_{i=0}^{\infty} a_i (1-\lambda_i)^n \psi_i(\underline{k}) \qquad (2.16)$$

which is identical to that obtained by Papoulis [39] for the case of one-dimensional signals. This error tends to zero as $n \to \infty$.

signal from each end of the delay line. The time interval between arrival of the pulse on the anode wires and that of the delayed signal at each end of the delay line is measured. If the gamma generates a pulse at only one location of the detector assembly, the sum of the intervals to each end should equal the length of the delay line plus some fixed delay in the processing electronics, a constant to within the accuracy of the timing measurements. Figure 3.1 shows the time sum distribution for an Fe^{55} source whose 5.9 keV photon, being stopped entirely within the chamber, did not interact with the converter. As expected for a single interaction type event, the distribution is symmetrical and narrow with a 5 nsec FWHM. In the case of multiple signals, however, the sum of the 2 intervals will be some value less than the length of the line, and thus these events can be distinguished and rejected. One additional advantage of reading from both ends is that in the case where the accuracy is limited by timing errors, averaging the positions obtained from each end of the line improves the resolution by a factor of $\sqrt{2}$.

To illustrate this effect we measured the time sum distribution for a point source of Ge^{68}, a positron emitter. A small NaI detector was used in coincidence with the prompt signal from the anode plane to provide a well collimated beam of 511 keV photons (from the geometry the size of the beam at the converter was approximately 3mm). In Fig. 3.2 an x-projection of the detector point response function for the positron source is plotted with accidental background subtracted. In all cases discussed here accidental background is removed by applying identical

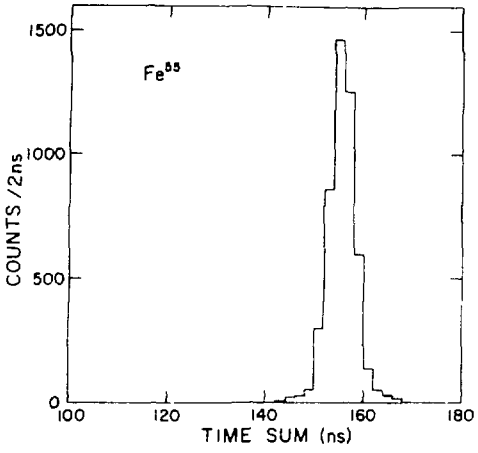

Fig. 3.1. Time sum distribution for an Fe^{55} source.

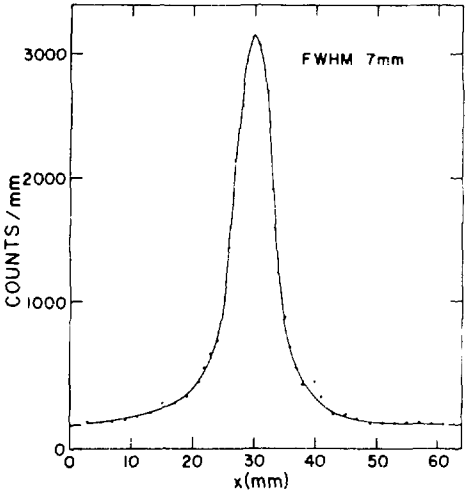

XBL 796-10279

Fig. 3.2. X-projection of detector point response function for the positron source.

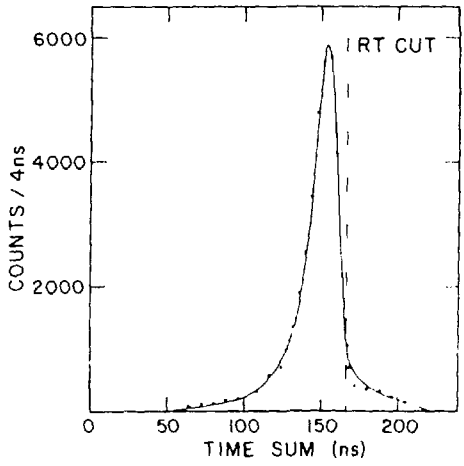

Fig. 3.3. Time sum distribution for the positron source. The cut on the high side of the peak is shown.

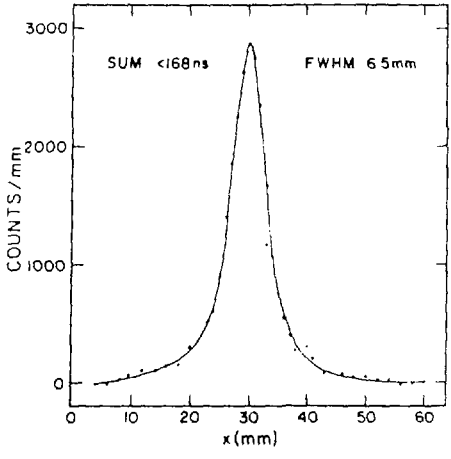

XBL 796-10278

Fig. 3.4. X-projection of detector point response function for those events with time sums less than 168 ns.

Table 3.1. The number of events contained in intervals about the mean of x-projection of the detector point response function for various time sum cuts. The fraction of those events passing the cut, which fall within the interval, is also given.

Interval	No Sum Cuts	Sum <168 ns	141<Sum<168 ns	150<Sum <168ns
5 mm	14003	12495	11481	8464
	49%	50%	65%	72%
10 mm	21604	19105	15057	10655
	75%	77%	86%	91%
15 mm	24867	21942	16472	11346
	86%	88%	94%	97%

A Monte Carlo program was written to determine the probability of secondary interactions from photoelectric escape photons and Compton scattering, and their contributions to the spatial resolution. The 511 keV photon was assumed to enter the converter perpendicularly. The material in the converter was assumed to be distributed uniformly throughout its volume. The point at which the 511 keV photon converted was sampled and an average detection probability was assigned. The conversion electron was considered detected if it escaped from the wall of the honeycomb into the gas. The Compton scattered photon or the 88 keV escape photon for Pb was followed until it converted or escaped from the converter. The program successful predicted the detection efficiency of the converter to within 20% of the experimental value. However, it showed that the probability of having a multiple event due to scattering is only 4%, which is not enought to explain the effect observed. This

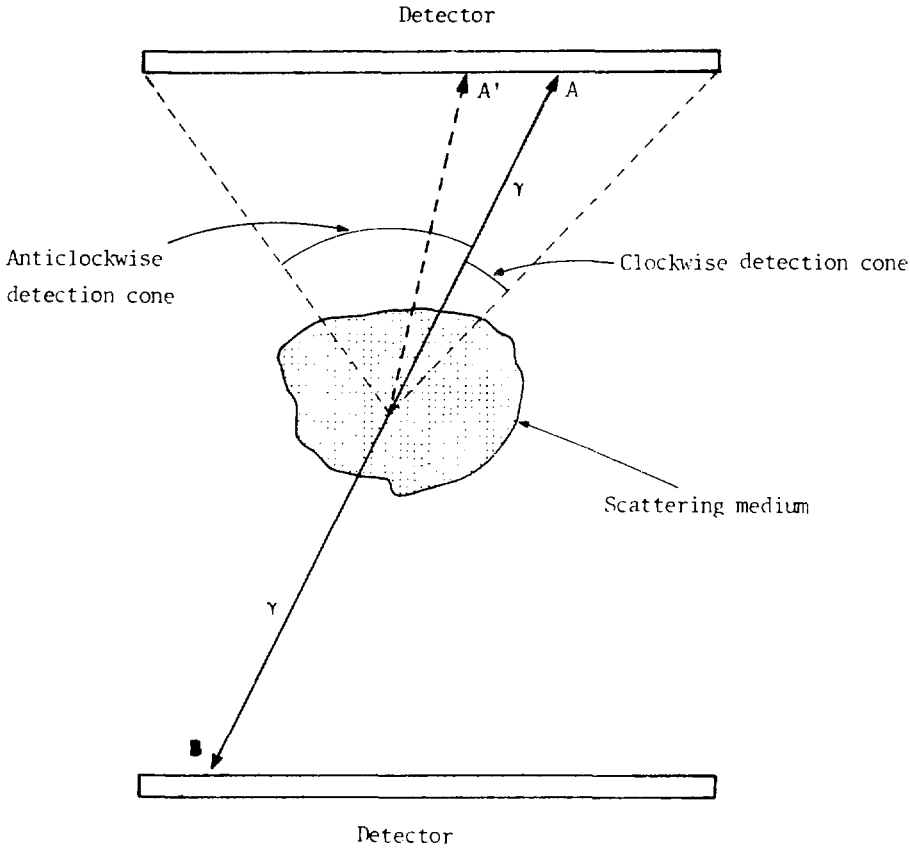

XBL 7911-12682

Fig. 3.7. Effect of scattering on the angle of the detected annihilation gamma pair.

results are displayed in Fig. 3.8. The two solid histograms show the angular distributions for a point source in air and that for a point source located at the center of a sphere of water medium of radius 10 cm. The total number of events generated is equal in the two cases. For the point source in water, the portion of events that were unscattered is shown as the broken histogram. No scattering was assumed in the positron camera in both cases.

We have also studied the angular distributions of the events taken from the MWPC-gamma converter positron camera (see Sec. 4.1). The two histograms in Fig. 3.9 show the angular distribution of annihilation gammas from a point Cu source in air and one embedded in a bucket of water respectively. Again, it can be seen that those events scattered by water are more populated at small angles. The fact that the distribution for the source in air is also peaked in the small angle region, though to a much smaller extent, is attributed to scattering in the detectors.

Knowing that the scattered events occur more at small angles, data can be filtered to put more emphasis on the large-angle events. Such filtering can be achieved through the use of those angular factors $F(\theta)$ in equation (2.9) which peak at large θ, such as $\cos^{-n}\theta$, $\sin^{n}\theta$, etc., where n is a positive integer.

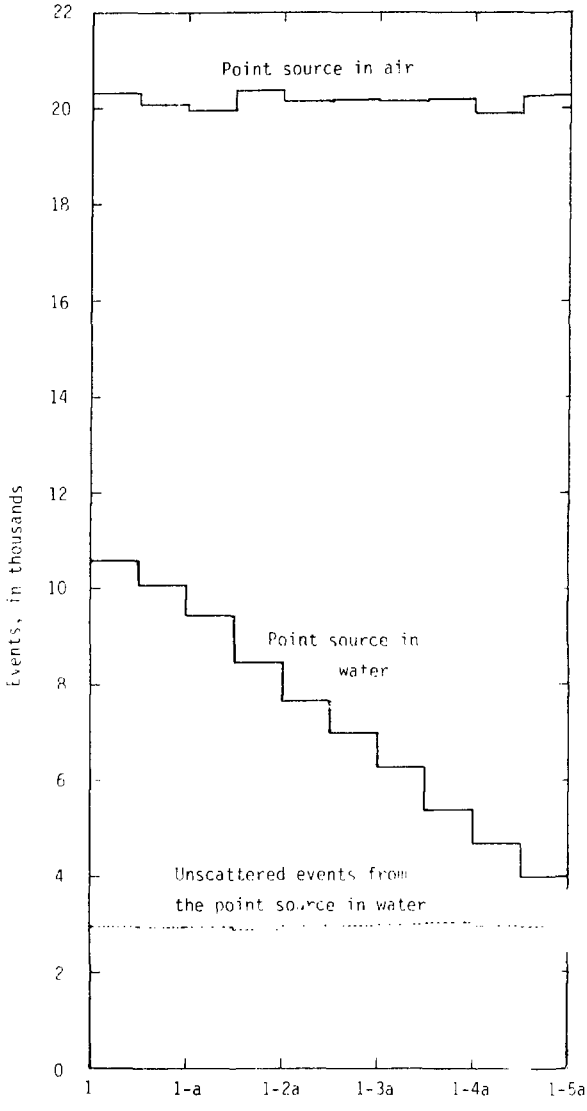

Fig. 3.8. Angular distributions of the simulated detected events from 2 point sources: one in air and the other in a sphere of water.

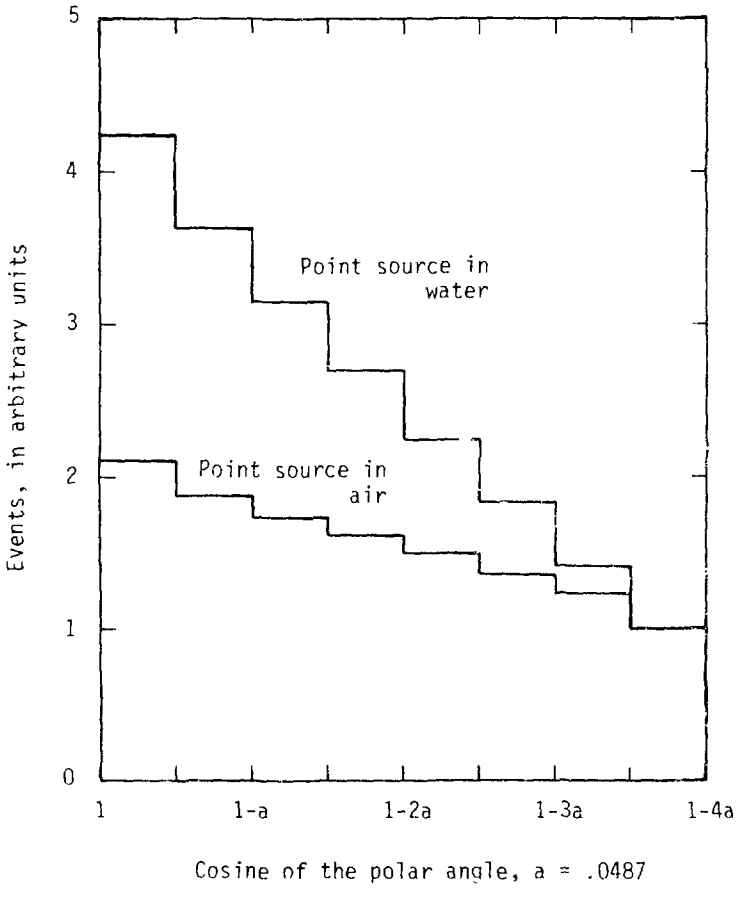

XBL 796-10277

Fig. 3.9. Angular distributions of the real detected events from 2 point sources: one in air and the other in a bucket of water. The two histograms have been normalized at the right-most bin.

3.2. Error Propagation and Stabilization in Reconstructions

As shown in Sec. 2.2, complete 3-D reconstructions can be achieved through deconvolution followed by iterations, or through matrix inversion. In this section we formulate the propagation of errors in each of these two approaches, and develop methods to stabilize their performance in the presence of noise.

3.2.1. Deconvolution Followed by Iterations

The deconvolution method solves for $R(\underline{k})$, the Fourier components of $\rho(\underline{r})$. If noise $N(\underline{k})$ is present in the data $T(\underline{k})$, the propagated error $E_d(\underline{k})$ in the reconstruction will be given by

$$E_d(\underline{k}) = \frac{N(\underline{k})}{T_0(\underline{k})}, \qquad T_0(\underline{k}) \neq 0. \tag{3.1}$$

Equation (3.1) shows that the error in the data is multiplied by the factor $1/T_0(\underline{k})$ in deconvolution. In the region where $T_0(\underline{k})$ is very small, the error will be greatly magnified. This is the case in the missing cone as well as in the high $|k_x|$ region, since equation (D.2) shows that for fixed $|k_z|/|k_x|$, $T_0(\underline{k}) \sim 1/|k_x|$.

In the iterative scheme (2.15), $R(\underline{k})$ is set to zero in the missing cone before iterating. This procedure removes the instabilities there. A way to deal with the instabilities in the high $|k_x|$ region has been described by Phillips [42]. However, we shall recast his treatment, since the convolution integral permits a particularly elegant realization of the technique.

Suppose the scalar field $\phi(\underline{r})$ is known only up to some error $\epsilon(\underline{r})$. Then, the equation to be solved is,

$$\phi(\underline{r}) + \epsilon(\underline{r}) = \int d^3r' \phi_0(\underline{r}-\underline{r}')\rho(\underline{r}') \tag{3.2}$$

where the error $\epsilon(\underline{r})$ is an arbitrary function except for some condition on its magnitude, such as $|\epsilon(\underline{r})| \leq M$. Equation (3.2) may be solved for $\rho(\underline{r})$ by taking the Fourier transform,

$$\rho(\underline{r}) = \int d^3r' [\rho(\underline{r}') + \phi(\underline{r}')] \int d^3k \frac{\exp[-2\pi i \underline{k}\cdot(\underline{r}-\underline{r}')]}{\Phi_0(\underline{k})} .$$

The functional derivative of $\rho(\underline{r})$ with respect to $\epsilon(\underline{r}')$ is a function of $\underline{r}-\underline{r}'$,

$$\frac{\delta\rho(\underline{r})}{\delta\epsilon(\underline{r}')} = \int d^3k \frac{\exp[-2\pi i \underline{k}\cdot(\underline{r}-\underline{r}')]}{\Phi_0(\underline{k})} = \alpha(\underline{r}-\underline{r}'). \tag{3.3}$$

The error tends to be random from point to point, and it generates instabilities in the solution $\rho(\underline{r})$ which are manifested as sharp fluctuations. Thus, a reasonable condition on $\rho(\underline{r})$ is a requirement for smoothness, in which a solution is sought such that

$$\int d^3r \, [\nabla^2 \rho(\underline{r})]^2 = \text{minimum} . \tag{3.4}$$

Suppose the total error is some fixed number e where

$$e^2 = \int d^3r \, [\epsilon(\underline{r})]^2. \tag{3.5}$$

Then the smoothness condition may be re-expressed by introducing a Lagrange multiplier $1/\gamma$ and minimizing the following expression with respect to variations in $\epsilon(\underline{r})$:

$$\int d^3r\,[\nabla^2\rho(\underline{r})]^2 + \frac{1}{\alpha}\int d^3r\,\rho(\underline{r})^2.$$

It is clear that α must be non-negative, if there is to be a meaningful solution. The functional derivative of this expression with respect to $\rho(\underline{r}')$ gives an expression for the smoothness condition on the solution $\rho(\underline{r})$,

$$0 = \alpha\int d^3r\,\nabla^2\rho(\underline{r})\nabla^2\frac{\delta\rho(\underline{r})}{\delta\rho(\underline{r}')} + \rho(\underline{r}')$$

subject to the constraint, equation (3.5).

Integration by parts and use of equation (3.3) yield an expression for the error which is proportional to α,

$$\rho(\underline{r}) = -\alpha\int d^3r'\,\rho(\underline{r}')G^{-1}(\underline{r}'-\underline{r}) \qquad (3.6)$$

where

$$G^{-1}(\underline{r}'-\underline{r}) = (2\pi)^{-3}\int d^3k\,\frac{k^4}{\rho_0(\underline{k})}\exp[-2\pi i\underline{k}\cdot(\underline{r}'-\underline{r})].$$

Substituting equation (3.6) into equation (3.2) gives a new convolution equation,

$$\int d^3r'[\rho_0(\underline{r}-\underline{r}') + \alpha G^{-1}(\underline{r}'-\underline{r})]\,\rho(\underline{r}') = \rho_0(\underline{r}).$$

The solution for the density distribution in frequency space is simply

$$R(\underline{k}) = \frac{\rho_0(\underline{k})}{\rho_0(\underline{k}) + \alpha(2\pi)^{-3}k^4} \qquad (3.7)$$

while the error is expressed in terms of the Lagrange multiplier

$$\rho(\underline{r}) = -\alpha(2\pi)^{-3}\int d^3k\,\exp(-2\pi i\underline{k}\cdot\underline{r})\,k^4\frac{R(\underline{k})}{\rho_0(\underline{k})}.$$

As for the iterative scheme (2.13), the rate of convergence, i.e., the rate $E_t^{(n)}$ goes to zero, depends on the distribution of $\{\lambda_j\}$ and $\{a_i\}$. The distribution of $\{\lambda_j\}$ is determined by the regions R_a and R_b. In general the region R_b, which represents the extent occupied by the object, is fixed, whereas the region R_a can be changed by varying the angle subtended by the imaging device.

Figure 3.10 shows a plot of the eigenvalues for various opening angles of R_a while R_b is chosen to be a 9×9 square sub-lattice in a 21×21 reconstruction lattice. It can be seen that the spectrum shifts towards zero as the angle decreases. The implication is that the convergence as expressed by equation (2.16) will become worse when the angle of R_a is reduced.

To show this effect we applied the iterative algorithm to restore the missing-cone components for a 2-D phantom. The reconstruction area is a 128×32 lattice, with equal lattice spacings in the x(i) and z(k) directions. The phantom has a square boundary with perpendicular diagonals which are both 11 lattice spacings long in the x and z directions, respectively. The Fourier components of the phantom outside the allowed cone were first set to zero, and then the iterative scheme was employed to recover them. The solid curve in Fig. 3.11 shows the root mean square error σ of the results after 20 iterations as a function of the half-angle of R_a. Here σ is defined as

$$\sigma = \sqrt{\frac{\sum_{i,j,k} (\text{reconstruction } (i,j,k) - \text{phantom } (i,j,k))^2}{\text{total number of picture elements}}} \qquad (3.9)$$

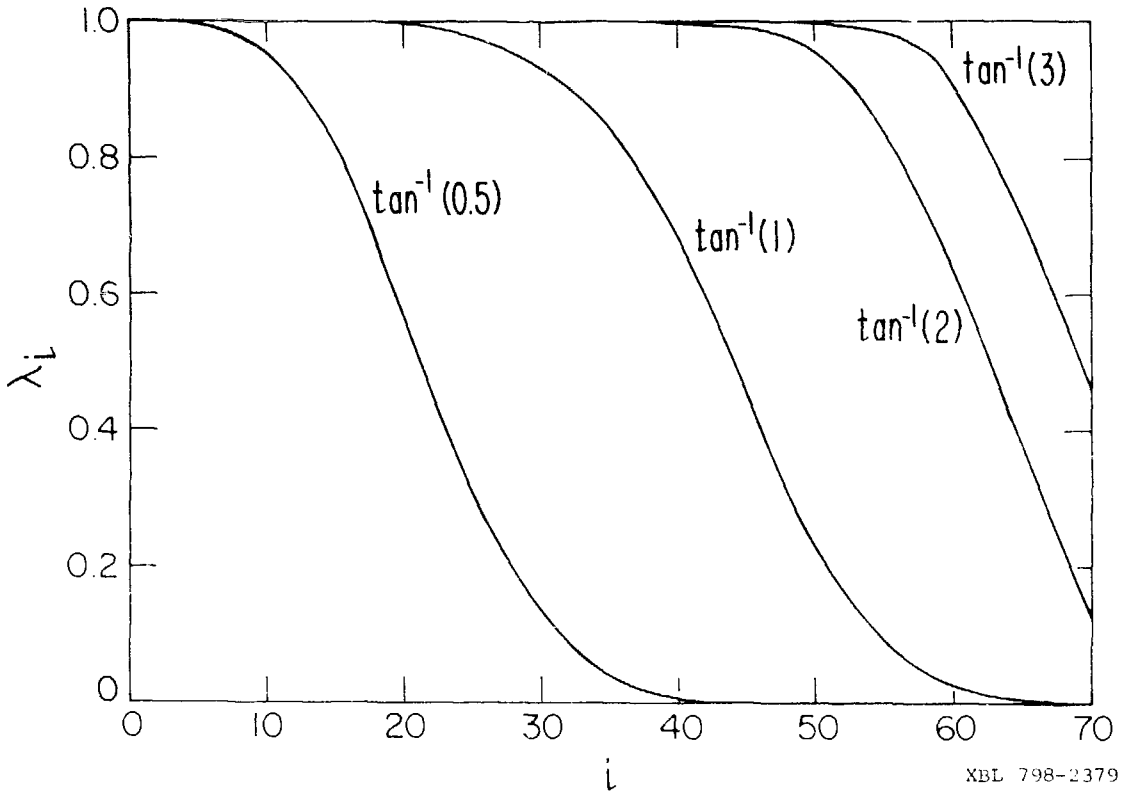

Fig. 3.10. Eigenvalues of BA for a two-dimensional problem for various semi-vertical angles of the allowed cone.

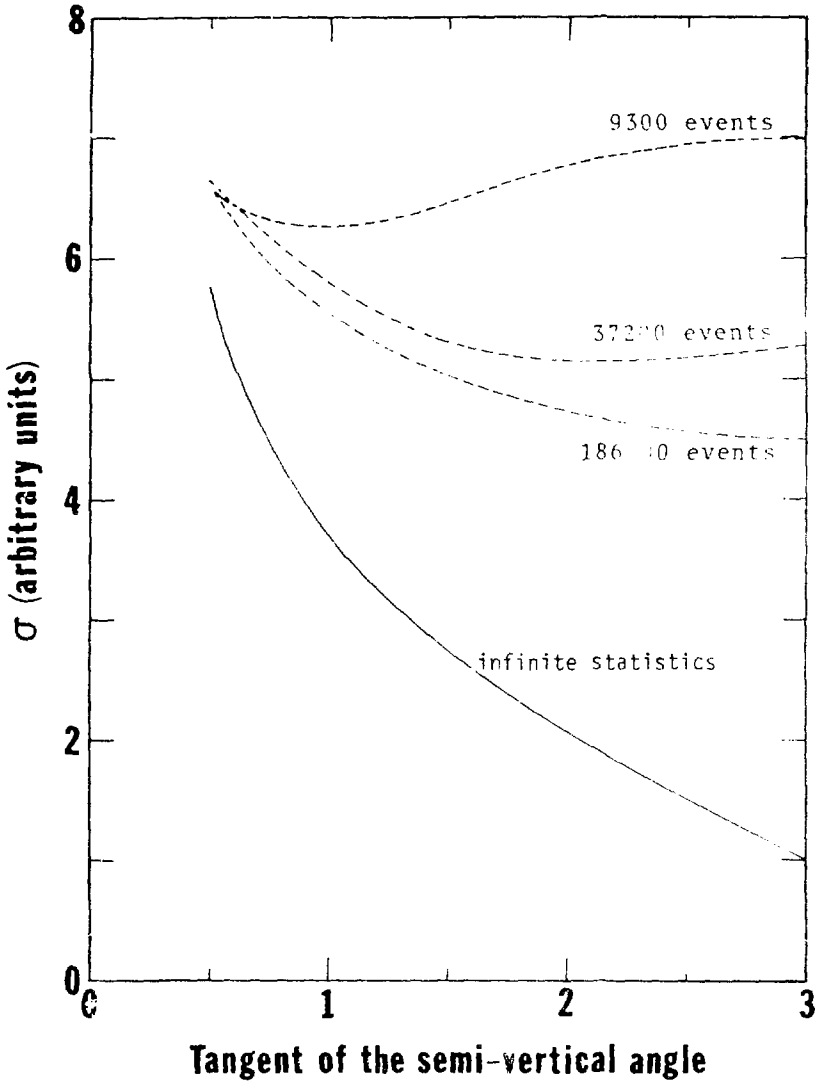

XBL 798-2378

Fig. 3.11. Root mean square error in reconstruction a 2-D phantom as a function of the semi-vertical angle of the allowed cone for various statistics.

Figure 3.12 shows the corresponding results for a three-dimensional phantom. The shape of the point response function ϕ_0 was in the form of a square pyramid with semi-vertical angle θ_0 (Fig. 2.19A). These two results show clearly the dependence of the truncation error $E_t^{(n)}(\underline{k})$ on the size of the opening angle of the allowed cone.

The above results can be viewed as reconstructions from perfect data generated by the phantoms, using deconvolution + iterations. For comparison, deconvolution + iterations were performed on a number of sets of finite statistical positron annihilation events generated by the 2-D phantom. The values of ε for these results are plotted as the broken curves in Fig. 3.11. It can be seen that the truncation error is the main source of error at small angles of R_a, whereas the statistical error dominates at large angles. The minimum in ε which occurs for finite statistical reconstructions is due to the competition of two effects: the improvement in the behavior of the eigenvalues $\{\lambda_i\}$ on the one hand, and the increase in the error magnitude of $\phi(\underline{r})$ on the other, as the angle increases while keeping the number of annihilation events fixed.

Besides the truncation error $E_t^{(n)}$, the measured error $\Delta S(\underline{k})$ in the frequency components in the allowed cone R_a also propagates in the iterations. Following Papoulis [39], we expand $\Delta S(\underline{k})$ in a series of eigenfunctions of BA in the region R_a

$$\Delta S(\underline{k}) = \sum_{i=0}^{\infty} c_i \psi_i(\underline{k}) \qquad \underline{k} \in R_a$$

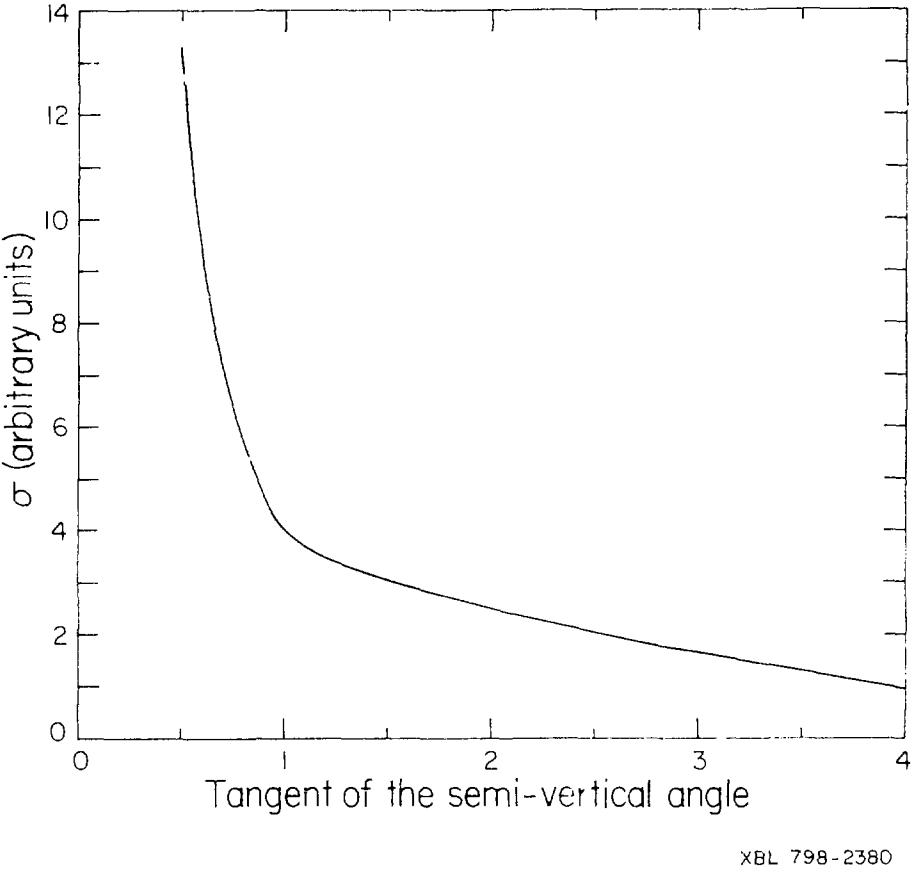

Fig. 3.12. Root mean square error after 20 iterations as a function of the semi-vertical angle of the allowed cone for a three-dimensional phantom.

$$p(k_x,z) = \sum_i \frac{(g_i^*, \varphi)}{\lambda_i} g_i(k_x,z)$$

where λ_i, g_i are the eigenvalues and eigenfunctions of the integral operator (2.8a), and

$$(g_i^*, \varphi) = \int_{-\infty}^{\infty} g_i^*(k_x,z)\, \varphi(k_x,z)dz.$$

If the data $\varphi(k_x,z)$ contain error $\Delta\varphi(k_x,z)$, then the propagated error in inversion E_m will be given by

$$E_m(k_x,z) = \sum_i \frac{(g_i^*, \Delta\varphi)}{\lambda_i} g_i(k_x,z). \tag{3.10}$$

Again, the expression (3.10) shows that the major errors in the reconstruction come from the small eigenvalues.

Now φ_0 is of the form (see Sec. 2.2.3.2)

$$\varphi_0(k_x,z-z') = \int_{-\theta_0}^{\theta_0} \frac{F(\theta)}{\pi} \exp\{2\pi i k_x \tan\theta(z-z')\}d\theta.$$

For the particular case $F(\theta) = \cos^{-2}\theta$ inside the detection cone, the expression for φ_0 simplifies to

$$\varphi_0(k_x,z-z') = \frac{1}{\pi}\int_{-\theta_0}^{\theta_0} \exp\{2\pi i k_x \tan\theta(z-z')\}d(\tan\theta)$$

$$= \frac{\sin[2\pi k_x \tan\theta_0(z-z')]}{\pi^2 k_x(z-z')}.$$

The eigenvalue equation of this kernel is

$$\lambda_i g_i(k_x,z) = \int_{z_1}^{z_2} g_i(z) \frac{\sin[2\pi k_x \tan\theta_0(z-z')]}{\pi^2 k_x(z-z')} dz'. \tag{3.11}$$

On rearranging equation (3.11) becomes

$$(\pi k_x \lambda_i)\, g_i(k_x,z) = \int_{z_1}^{z_2} \frac{\sin(2\pi k_x \tan\theta_0 (z-z'))}{\pi(z-z')}\, g_i(k_x,z')dz'$$

which is the zeroth order prolate spheroidal eigenvalue equation. Thus $(\pi k_x \lambda_i)$ is a set of zeroth order prolate spheroidal eigenvalues. As pointed out in [35,43], the distribution of those eigenvalue depends on the quantity $c = 2\pi k_x \tan\theta_0 (z_2-z_1)$, as shown in Fig. 3.13, and for a fixed c the eigenvalues fall off to zero rapidly with increasing i once i exceeds $(2/\pi)c$. This means that noise multiplication would be especially serious whenever k_x, $\tan\theta_0$, or $(z_2 - z_1)$ becomes small.

One way to stabilize the method, for fixed $\tan\theta_0$ and (z_2-z_1), is to discard the results at small $|k_x|$ where the errors dominate, and, by making use of the finite extent of the object in the x dimension, fill in those values using the results obtained from the higher $|k_x|$ values through the iterative scheme shown in Fig. 3.14.

Another way to stabilize the matrix method is by means of the smoothing procedure proposed by Phillips [42] and Twomey [44]. Instead of solving the ill-conditioned matrix equation

$$Y = AX$$

which is the digital version of equation (2.8a), another matrix equation with a modified kernel

$$Y = (A + \gamma B)X$$

is solved. Here the matrix B is obtained from A in the following manner:

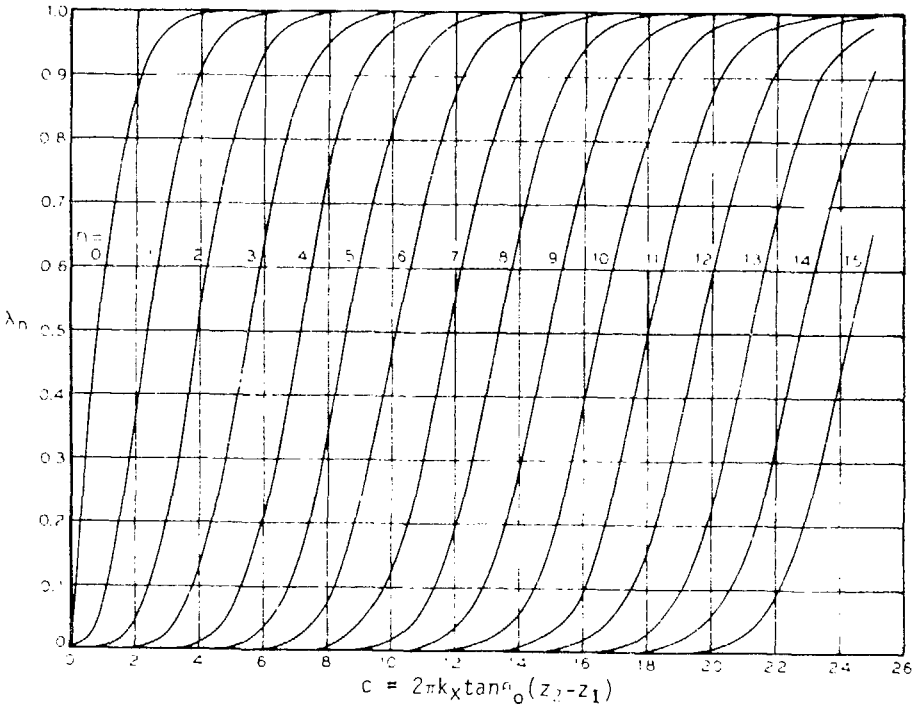

Fig. 3.15. Eigenvalues of the zeroth order prolate spheroidal equation.

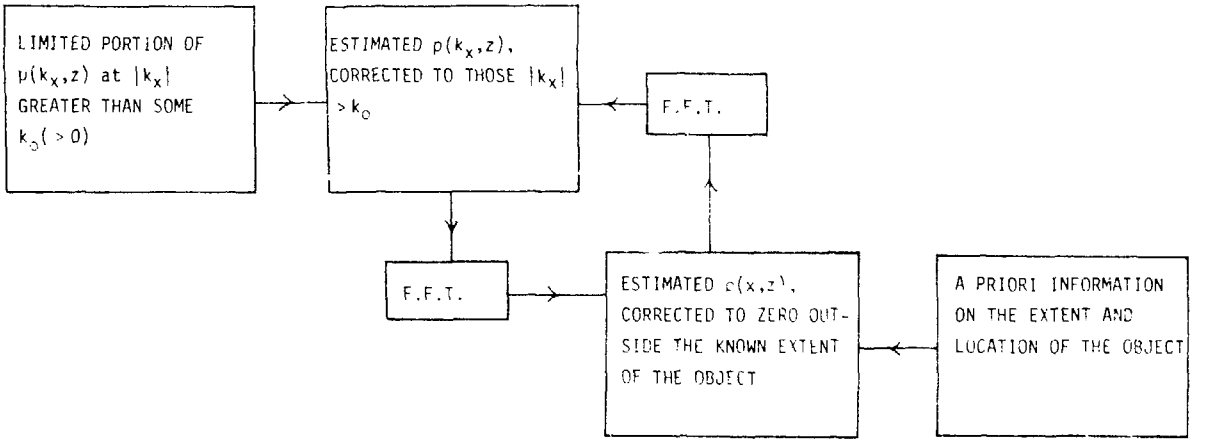

Fig. 3.14. Iterative scheme to stabilize the matrix inversion algorithm.

$$b_{z,k} = a_{k-2,z} - 4a_{k-1,z} + 6a_{k,z} - 4a_{k+1,z} + a_{k+2,z}$$

and γ is a parameter dependent on the noise level in the data. This procedure will remove the instabilities at the high spatial frequencies k_z for each of the operators (2.8a) characterized by different k_x.

3.2.3. Comparison between Deconvolution + Iterations and Matrix Inversion

After analyzing the basic properties of the deconvolution + iterations and the matrix methods, a comparison of their relative merit is now in order. If the data contain no error or only a negligible amount of error, the main error in the result of deconvolution + iterations will come from the truncation error $E_t^{(n)}$ in iterating, as the deconvolution error E_d will be insignificant in this case. For the matrix method, the inversion error E_m will also be negligible. The only unknown solution at $k_x = 0$ can be filled in by continuation from other non-zero k_x values, and the error introduced in continuing the solution to one point will be very small compared to the error $E_t^{(n)}$ in continuing the solution outside R_a for general half-angle α. Thus in the case of very small amounts of noise, the matrix inversion has an advantage over the deconvolution + iterations approach, unless some accelerated scheme can be devised to reduce $E_t^{(n)}$.

To predict their relative performance in the presence of significant amounts of noise, it suffices to compare the condition number of the deconvolution operation with that of the matrix inversion. For deconvolution, the condition number κ_d is given by

$$\kappa_d = \frac{(\Phi_0(\underline{k}))_{max}}{(\Phi_0(\underline{k}))_{min}} .$$

And for each $k_x \neq 0$, the condition number $\kappa_m(k_x)$ of the integral operator (2.8a) is given by

$$\kappa_m(k_x) = \frac{\alpha_{max}}{\alpha_{min}} .$$

Now equation (D.2) in Appendix D shows that $\Phi_0(\underline{k})$ is in the form

$$\Phi_0(k_x,k_z) = \frac{F(\theta_i)\cos^2\theta_i}{\pi|k_x|}$$

where $\tan\theta_i = - k_z/k_x$, and $F(\theta)$ is the angular factor used in constructing $\phi_0(\underline{r})$. For each $k_x \neq 0$, the condition number is thus given by

$$\kappa_d(k_x) = \frac{(F(\theta)\ \cos^2\theta)\ max}{(F(\theta)\ \cos^2\theta)\ min} .$$

In general the maximum and minimum values of $F(\theta)\ \cos^2\theta$ do not differ by several orders of magnitude; in fact, for the generally used angular factors $F(\theta) = 1$ and $F(\theta) = \cos^{-2}\theta$, $\kappa_d(k_x)$ equals $\sec^2\theta_0$ and 1 respectively. On the other hand, α_{max} and α_{min} can differ by a factor of order hundreds of thousands; in fact, α_i asymptotically approaches zero as the index of the eigenvalue increases, as shown in Appendix I. The decrease of α_i with the index is especially fast at small values of k_x and θ_0. Thus matrix inversion is expected to be more unstable to noise than deconvolution + iterations.

This comparison is still valid even if the iterative scheme in Fig. 3.14 is employed to stabilize the matrix method. The reason is the following. In iterating, all the solutions from inversion with $|k_x|$ below some $k_0 (> 0)$ are discarded, and they are filled in using those with $|k_x| \geq k_0$. But as the solution from inversion for every k_x contains both reliable and unreliable components corresponding to the large and small eigenvalues of the integral operator (2.8a) characterized by that k_x, the solutions used to start the iterations for the matrix method always contain some unreliable components. In contrast, the deconvolution results used to start iteration do not have unreliable components.

IV. IMPLEMENTATION

4.1. MWPC-Gamma Converter Positron Camera System

The MWPC-gamma converter positron camera system is shown in Fig. 4.1. The camera structure can be roughly divided into 3 parts, as illustrated in the block diagram in Fig. 4.2. The first group consists of MWPCs, gamma converters and delay lines for detecting the 511 keV annihilation gammas and localizing their positions of interaction. Next is the electronics system for signal processing. It includes low noise amplifiers, timing discriminators, a data selector unit, and an interface unit. The last group of hardware, which processes and stores the data, consists of a Digital Equipment Co. (DEC) PDP 11/20 computer with an extended memory of 28K, and peripherals including a display storage scope, two data storage disc units, a fast paper tape reader/punch, and a Decwriter keyboard terminal.

The sequence of data acquisition is as follows: On detecting a pair of annihilation gammas, 3 amplified signals from each detector (1 prompt anode signal and 2 delay line signals) are fed to multichannel timing discriminators. The 6 discriminator outputs are transmitted to the data selector logic unit which performs decision logic functions such as valid coincident event selection and invalid event inhibit/reset. At the same time the anode signals initiate 4 digitizing scalers which are stopped later by the delay line signals. If the event satisfies some data selection requirements (to be described in Sec. 4.1.2), an interrupt signal is transferred via the buffer unit to the memory of the computer. Otherwise, an inhibit/reset signal is issued by the data

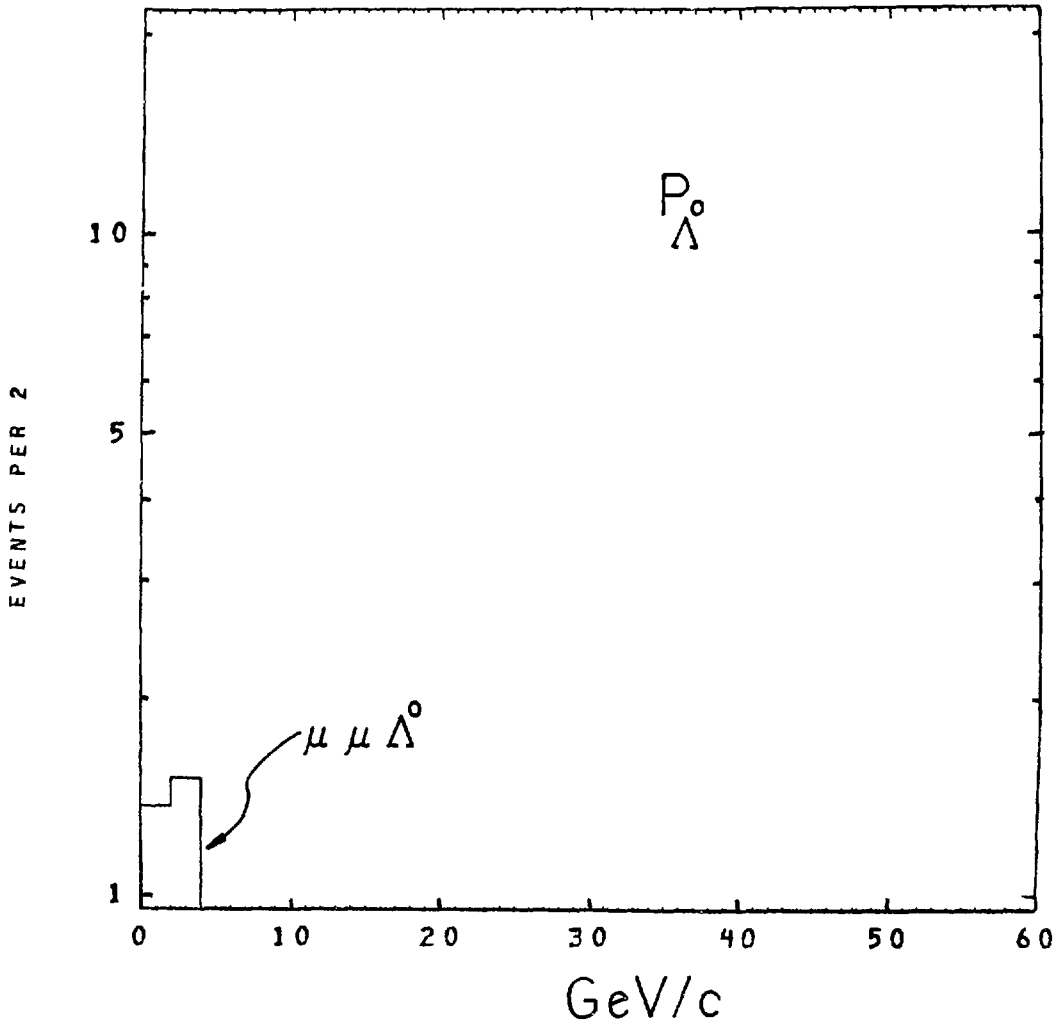
EVENTS PER 2
10
5
1
P_{Λ^0}
$\mu\,\mu\,\Lambda^0$
0
10
20
30
40
50
60
GeV/c

Fig. 7.28b

selector to all units. Some important components are described in detail in the following sections.

4.1.1. The Detection Assembly

Four MWPCs each with 48 cm × 48 cm sensitive area were used to form a pair of detectors, each of which was made up of 2 MWPCs and 2 Pb converters housed in an air-proof Al box. The cathode wires in each chamber were 50 μm in diameter and spaced 2 mm apart. They were terminated through 220 K_{Ω} resistors to a common bus. The anode wires were 20 μm in diameter and spaced 3 mm apart. The chamber frames were made of Nema G-10 fiberglass; the two central frames and the outer frames were each 4 mm thick. On these frames were epoxied the coupling strip PC boards. The delay lines were mounted on the coupling strips with 0.1 mm thick mylar between them and the strips for insulation. The detailed construction of the chamber is shown in Fig. 4.3.

The delay lines used were the phased compensated electromagnetic delay lines for wire chamber readout developed by Grove, Perez-Mendez, et al. [22,45]. The basic design, illustrated in Fig. 4.4, consists of a helical winding of #32 gauge copper Formvar wire on a plastic core with longitudinal copper bands on one side. A mylar strip with etched metallic bands of copper is cemented onto one of the flat sides of the delay line for phase compensation. The delay to rise time ratio is 28:1 and the total delay is 1.1 μsec.

The gamma converters were made of Pb shaped in the form of honeycomb, as shown in Fig. 4.5. The cell size is 3.5 mm and cell wall is 75 μm. The height of the converter is 15 mm. The detailed procedures

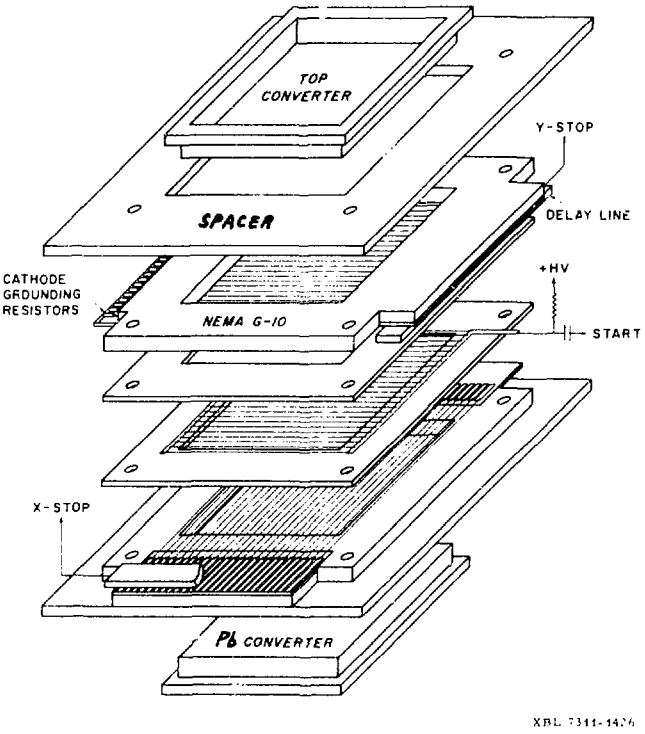

Fig. 4.3. Multiwire proportional chamber construction, the location of gamma converters is indicated.

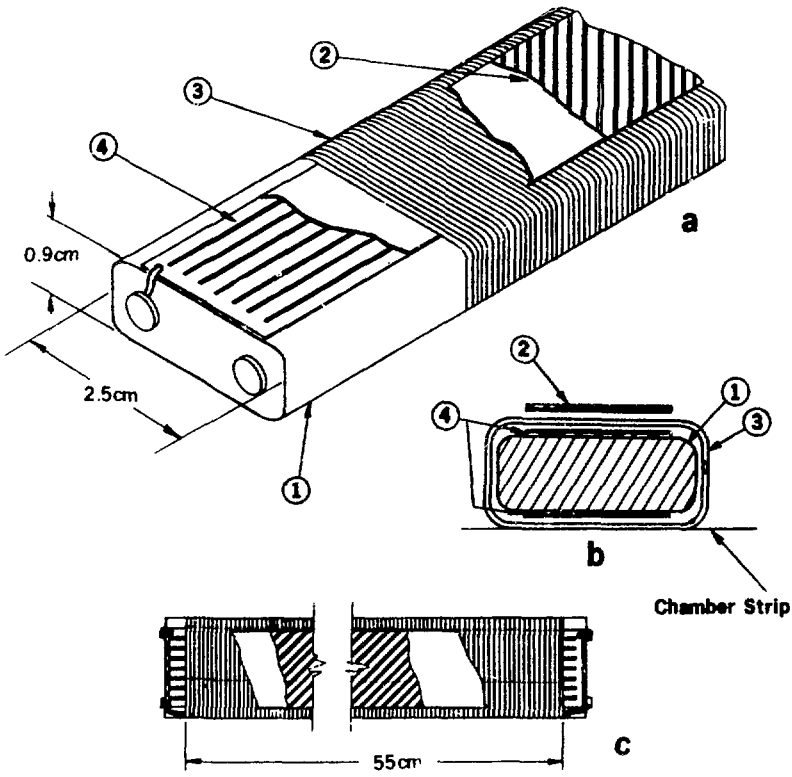

① Plastic Core

② Floating Metal Strips On Mylar Base: Strips = 1.8mm Wide; Gaps = 0.3mm Wide; Mylar = 25 Microns Thick

③ Winding = #30 Formvar Wire

④ 8 Copper Strips On Mylar Base: Strips = 1.8mm Wide; Gaps = 0.3mm Wide; Mylar = 25 Microns Thick

XBL 714-679

Fig. 4.4. MWPC delay line construction.

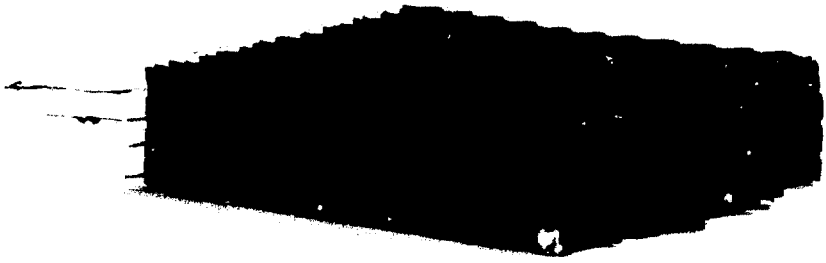

XBB 7410-7153

Fig. 4.5. A section of the layered, honeycomb shaped gamma converter. Graded voltages are applied through the bus-wires to individual cells.

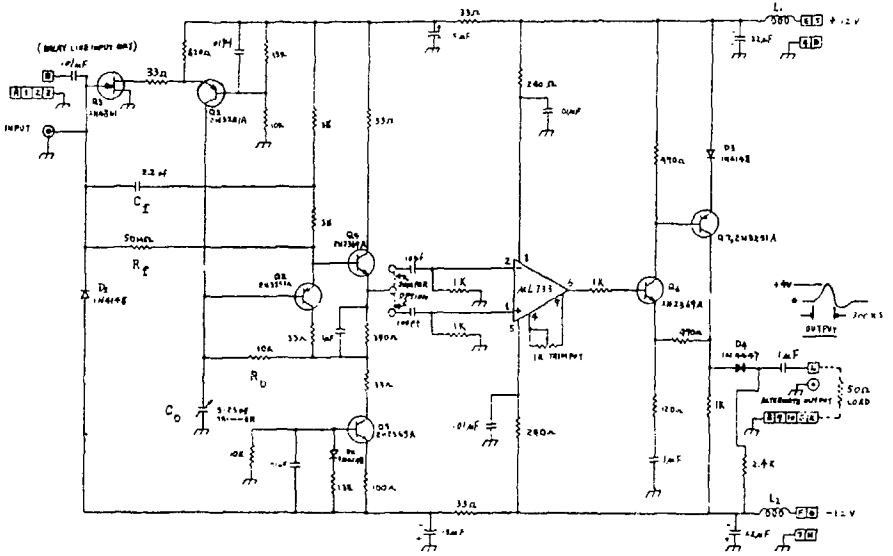

Notes: (1) All resistors 1/4 W, 5%, carbon unless otherwise noted.
(2) L_1, L_2 = 10 turns of #26 wire on 3E2A core.

Fig. 4.6. Schematic diagram of the Modified Charge-sensitive Amplifier.

XBL 796-10295

is common to a family of pulses, regardless of their amplitude [48].

The contributions to the timing inaccuracies include time slew which arises from the difference in pulse amplitude, and time jitter which is caused by the noise [49]. For the timing discriminator we used, the time slew is 6 nsec over a dynamic range of 20 in signal amplitude, and the time jitter associated with 100 mV signal and 20 mV noise is 8 nsec; but improves to 1 nsec as the input signal is increased to 1 V.

The Data Selector unit is made up of a network of flip-flops and gates to which the outputs from the timing discriminators are applied. Figure 4.7 shows its logic diagram. An event will be validated if it satisfies the following conditions:

Prompt anode signals

1. Only one of the two MWPCs is triggered in each of the upper and lower detector boxes (2 chambers were housed in one detector box).
2. When one of the two chambers in a detector box is triggered, the coincident signal from one of the chambers in the opposite detector box must arrive within the coincidence resolving time.

Delayed cathode signals

3. If conditions (1) and (2) in the prompt signals are met, there must exist 4 delayed cathode signals associated with the chambers which were triggered.

An event is rejected by the initiation of an inhibit/reset signal if,

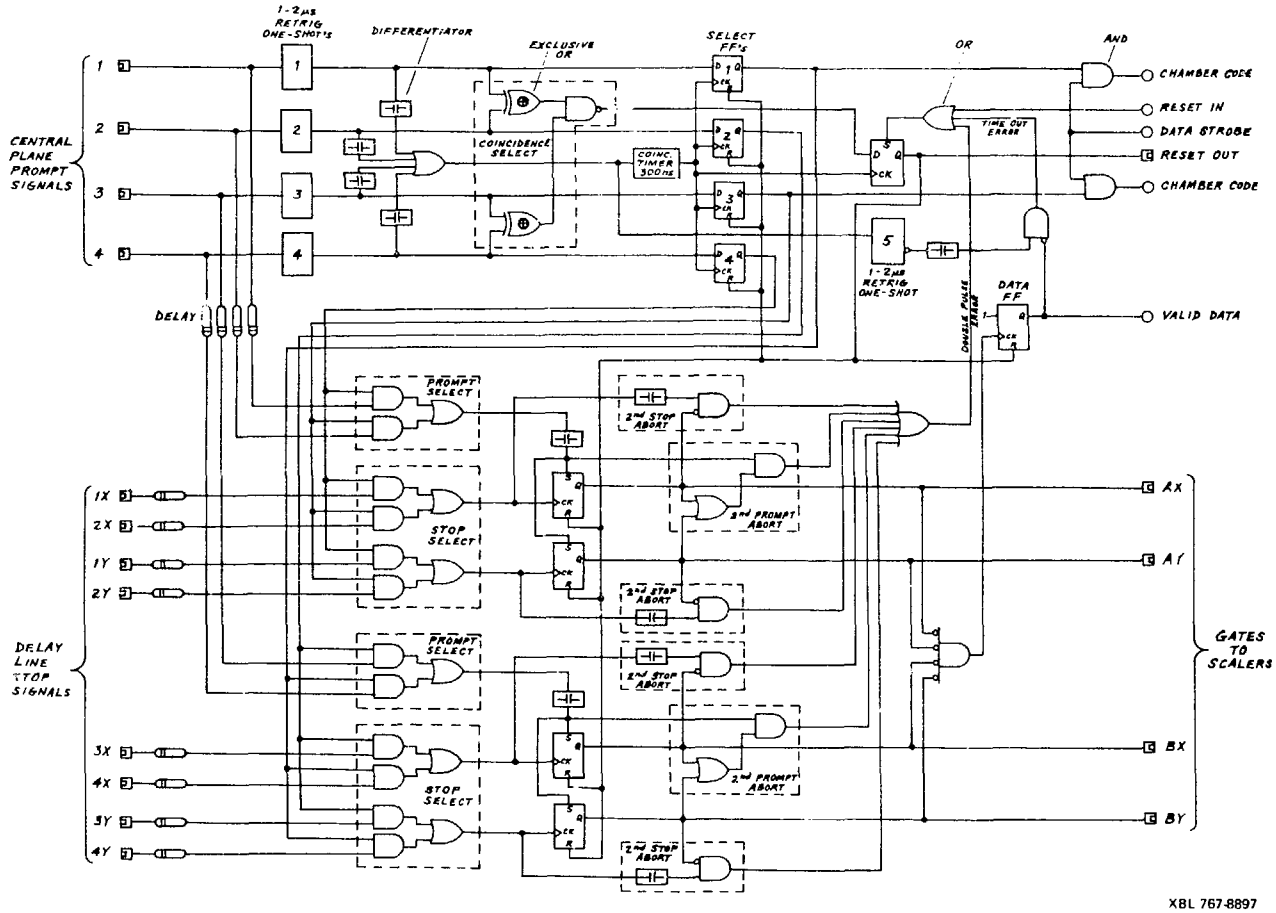

Fig. 4.7. Logic diagram of the data selector.

4. Any one of the conditions (1), (2), (3) is not satisfied.
5. A second prompt signal should occur on either one of the four chambers before a valid coincident signal is initiated.
6. More than one signal should occur on any one of the delay lines within delay line time (1.5 μsec) before a valid signal is initiated.

Whenever any one of the four MWPCs is triggered, further signals from that particular chamber would be gated off for 1.5 μsec while the other detectors are still operative. This would prevent accidental coincidence and minimize the detector system dead time.

4.2. Reconstruction Results

We have tested the results developed in Sections 2.2 and 3.2 by performing studies on some computer-generated phantoms and a real phantom. As the computations had to be done on digital computers, all the mathematical quantities were digitized on a finite-extent lattice with lattice spacings Δx, Δy, Δz, the choice of which is governed by the spatial resolution of the imaging device and the available core memory capacity of the computer. In digitizing we have restricted ourselves to frequency components below the maximum frequencies given by

$$k_x(\max) = \frac{1}{2\Delta x} \text{ , etc.}$$

The components at frequencies above this value were very small in magnitude as a consequence of the finite resolution, and were set to zero for computational purposes. The constraint that the density distribution is

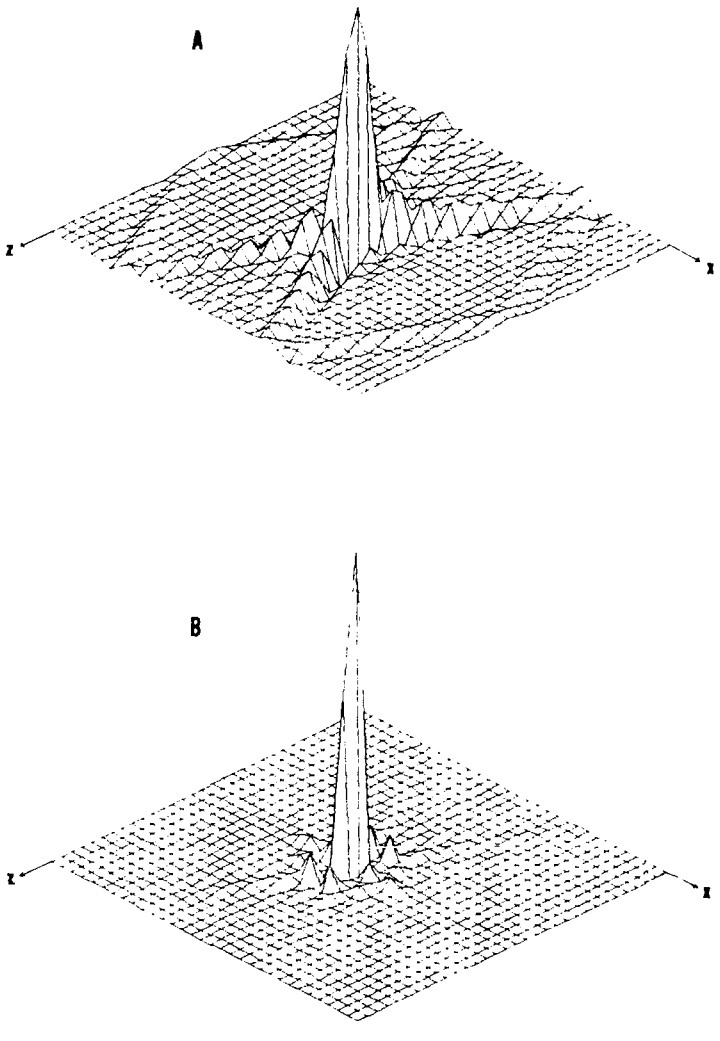

XBL 7910-12148

Fig. 4.8. Recovering the missing-cone components of a 2-D point source located at the center of a square which acts as the finite object extent in the iterations. The semi-vertical angle of the allowed cone is $\tan^{-1}(0.5)$.

(A) The point source with the missing-cone components set to zero.
(B) The point source after 30 iterations.

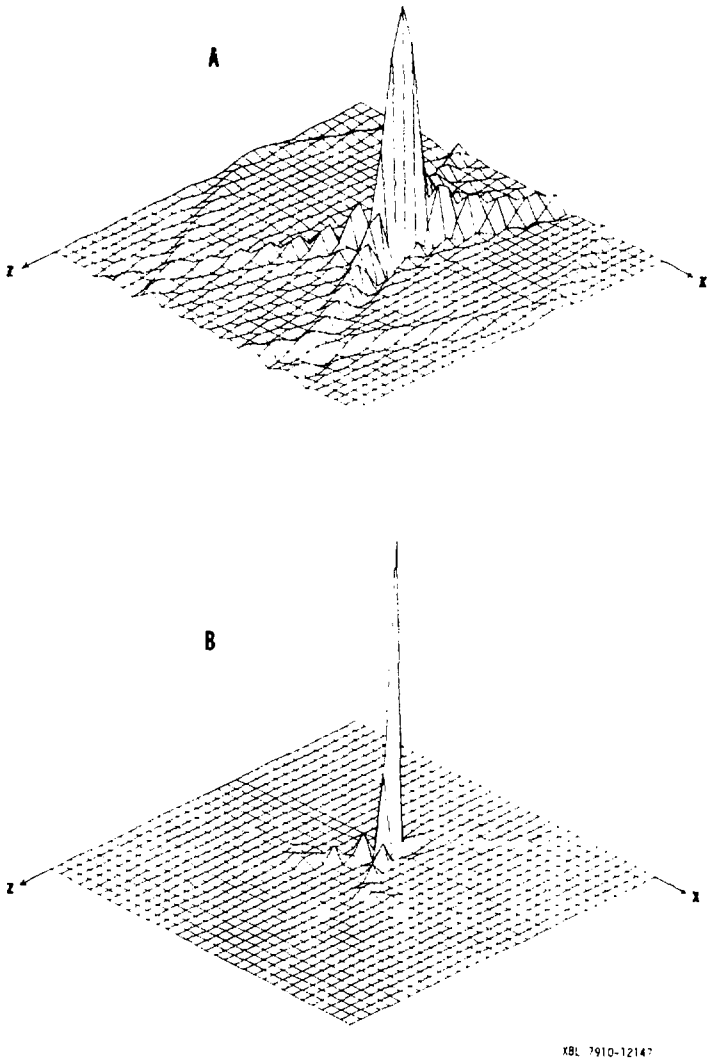

XBL 7910-12147

Fig. 4.9. Recovering the missing-cone components of a 2-D point source located on the boundary of a square which acts as the finite object extent in the iterations. The semi-vertical angle of the allowed cone is $\tan^{-1}(0.5)$.

(A) The point source with the missing-cone components set to zero.
(B) The point source after 30 iterations.

We then tested the effect of the size of the camera angle on deconvolution using the computer-generated 3-D phantom shown in Fig. 4.10, which was a spherical skull with a tumor located off-center inside. The skull was of inner radius 9 cm and thickness 2 cm, while the tumor had radius 1.5 cm. The concentration ratio was

tumor:skull:background = 10:5:1.

We performed reconstructions using the deconvolution method in three positron camera configurations with three different point response functions. The first point response function subtended a viewing angle (the solid angle of the detection cone in Fig. 2.19A) of one-third of 4π along the z-axis; the second one subtended two-thirds of 4π: one-third along the z-axis and the other third along the y-axis; and the last one had complete 4π viewing angle. The corresponded to camera configurations having one, two, and three pairs of detectors, respectively, with the axes joining each pair perpendicular to each other. The last configuration, though not very realistic practically, was included for making comparisons, because its point response function obviously contained no zero Fourier components. According to condition (2.11) in Sec. 2.2, the first point response function contained zero Fourier components, whereas the second one did not. The phantom generated a total number of 1.2 million events in each case. Reconstructions were done on a $48 \times 48 \times 48$ lattice, with lattice spacings 1 cm $\times$ 1 cm $\times$ 1 cm. Each event was weighted by $F(\theta) = \cos^{-3}\theta$ in constructing $\phi(\underline{r})$. $R(\underline{k})$ was set to zero wherever $\Phi_0(\underline{k})$ is zero or close to zero. The value of γ was set to zero in all the 3 deconvolutions.

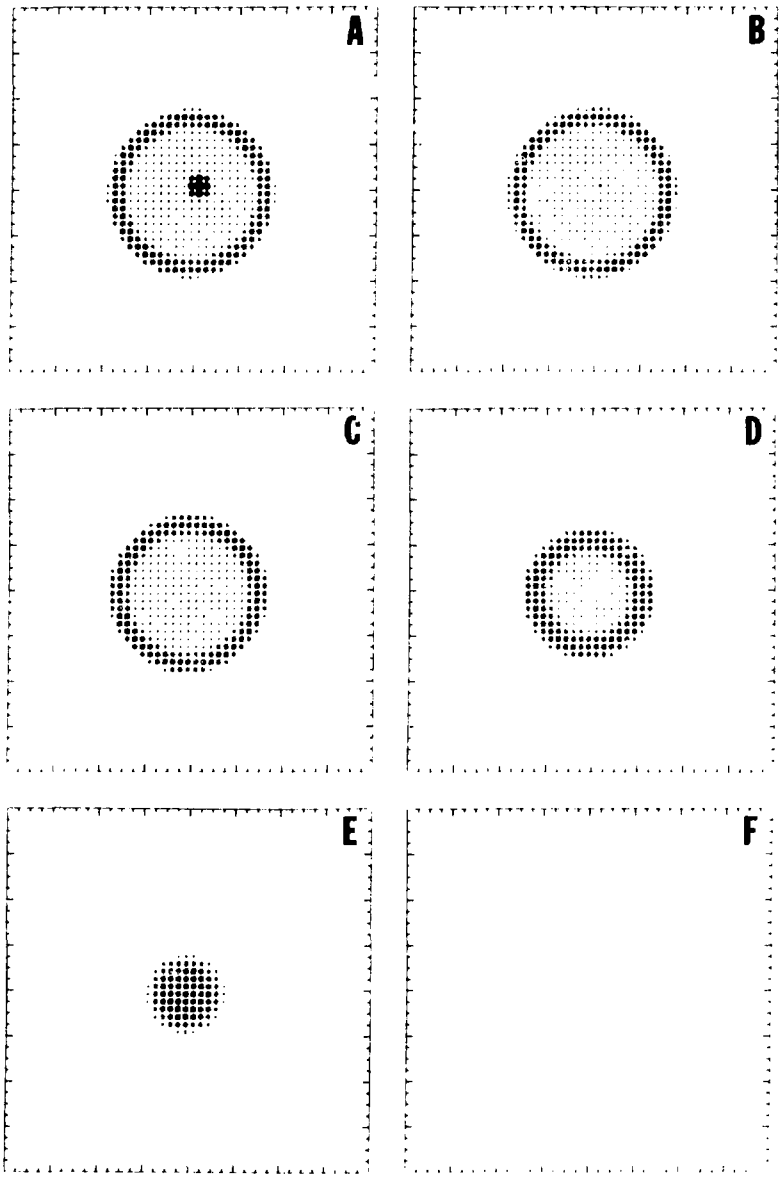

XBL 797-10701

Fig. 4.10. A computer-generated phantom simulating a brain tumor. The skull is 2 cm thick and has an inner radius of 9 cm. The tumor has a radius of 1.5 cm. The concentration is 5:1 for the skull and 10:1 for the tumor. Each picture element is 1×1 cm^2. The planes are 3 cm apart in the z direction.

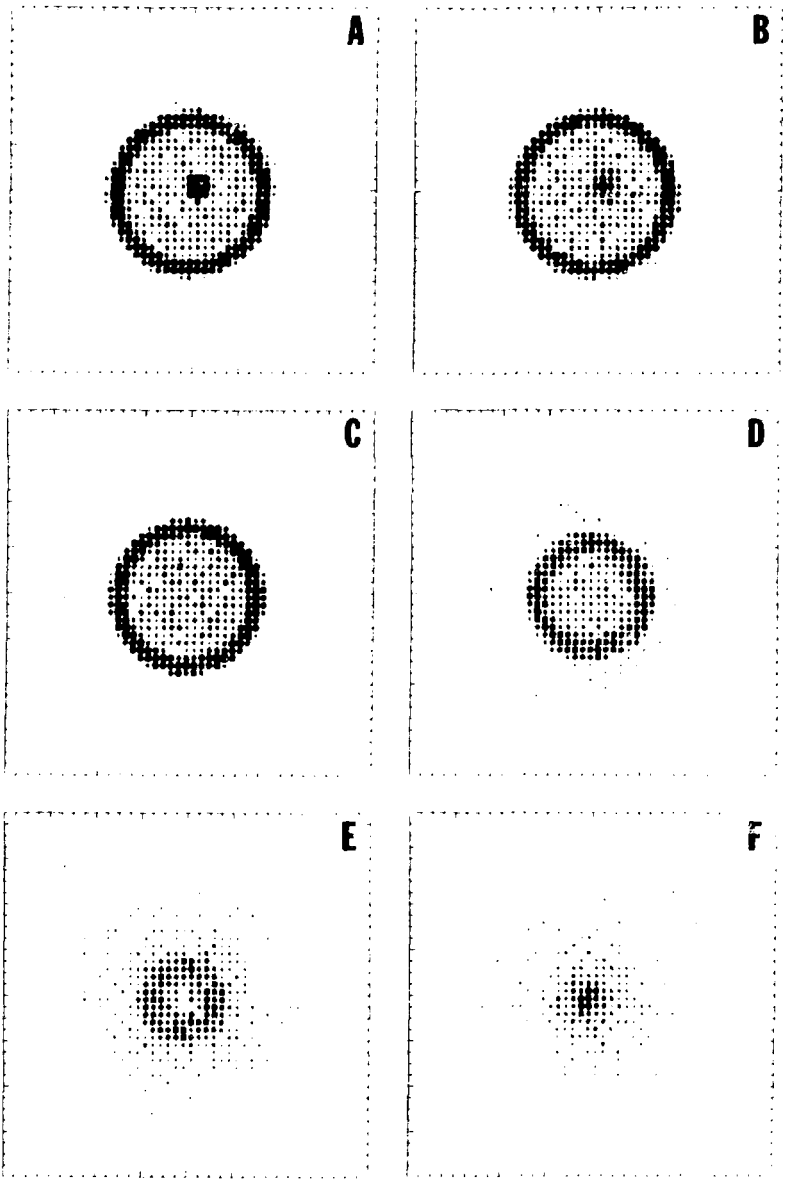

XBL 797-10704

Fig. 4.11. Deconvolved image in the two-sided camera having a point response function with viewing angle one-third of 4π along the z-axis. Each event is weighted by $\cos^{-3}\theta$ in constructing ϕ. The value of γ is 0.

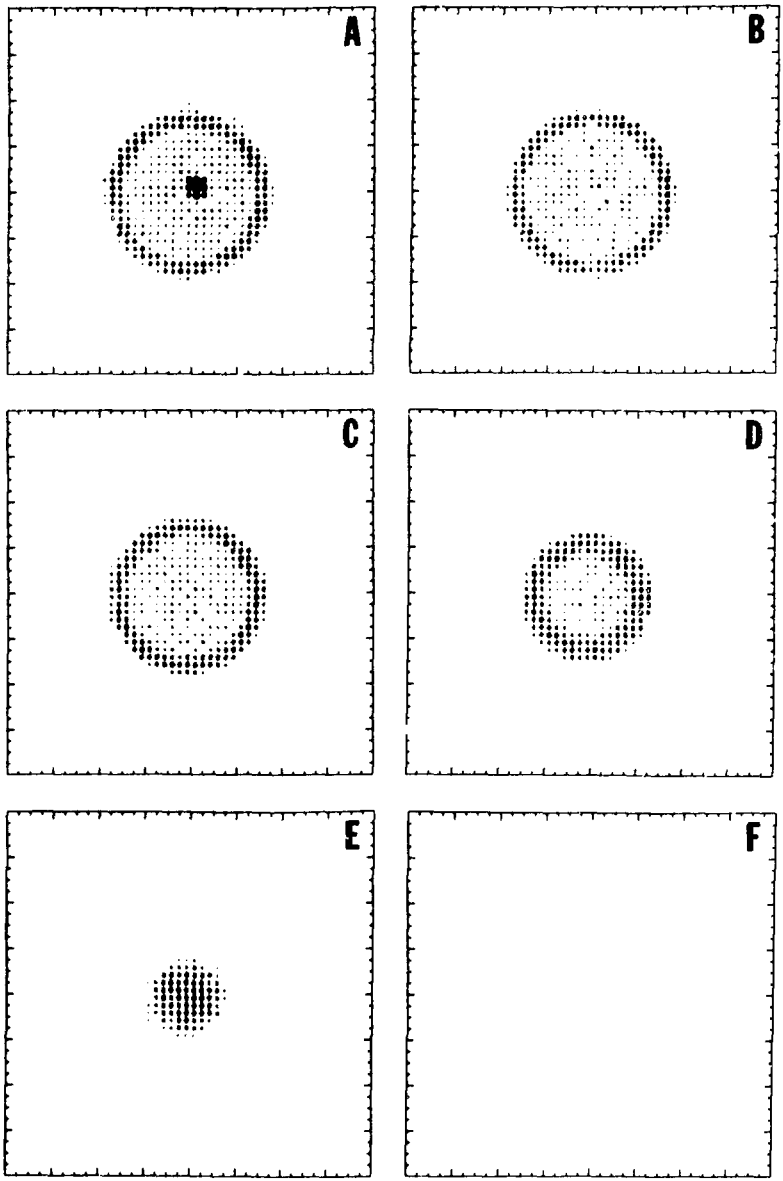

XBL 797-10706

Fig. 4.13. Deconvolved image in the six-sided camera having a point response function with complete 4π viewing angle. Each event is weighted by $\cos^{-3}\theta$ in constructing ϕ. The value of γ is 0.

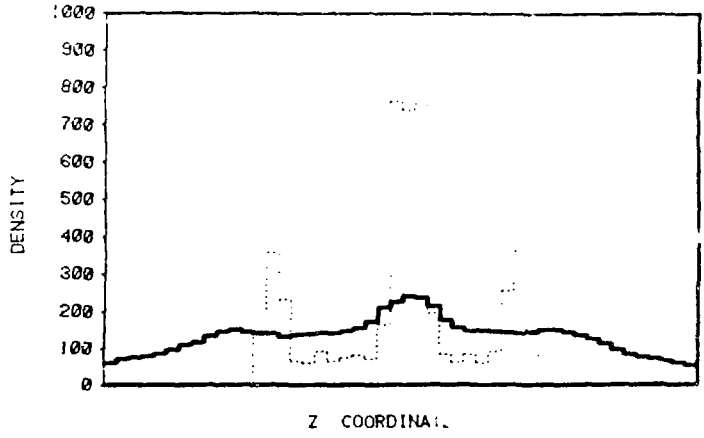

Fig. 4.15. Profile of the back-projection image in Fig. 4.14 along the line i = j = 25.

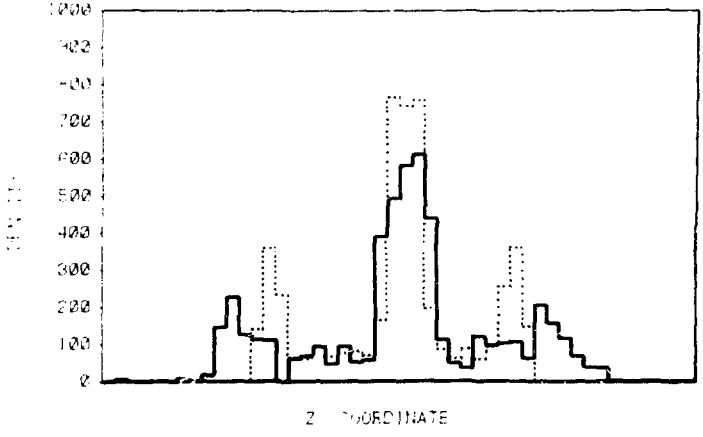

Fig. 4.16. Profile of the deconvolved image in Fig. 4.11 along the line i = j = 25.

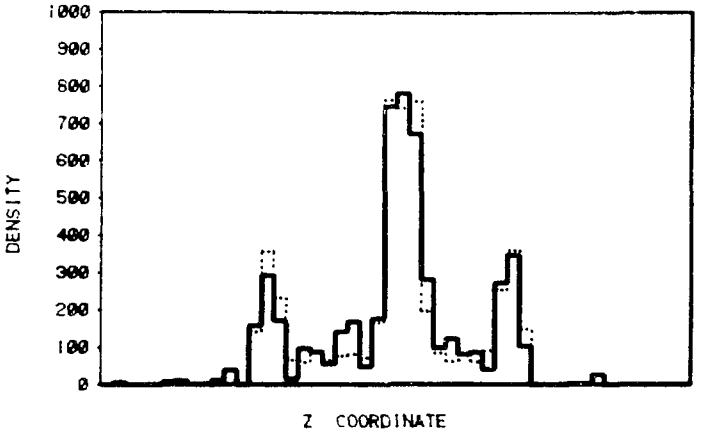

Fig. 4.17. Profile of the deconvolved image in Fig. 4.12 along the line i = j = 25.

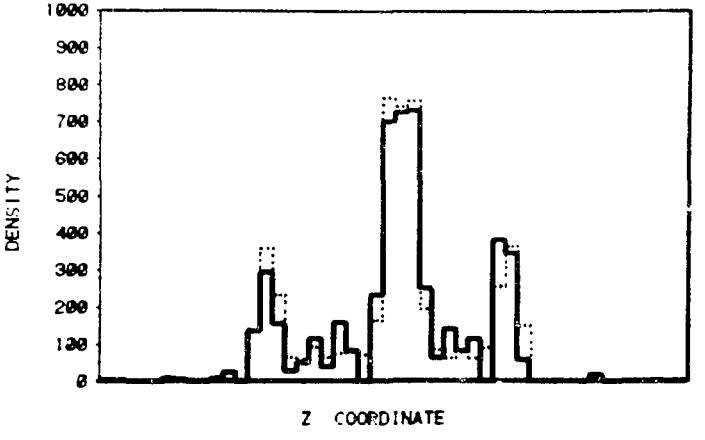

XBL 7910-12146

Fig. 4.18. Profile of deconvolved image in Fig. 4.13 along the line i = j = 25.

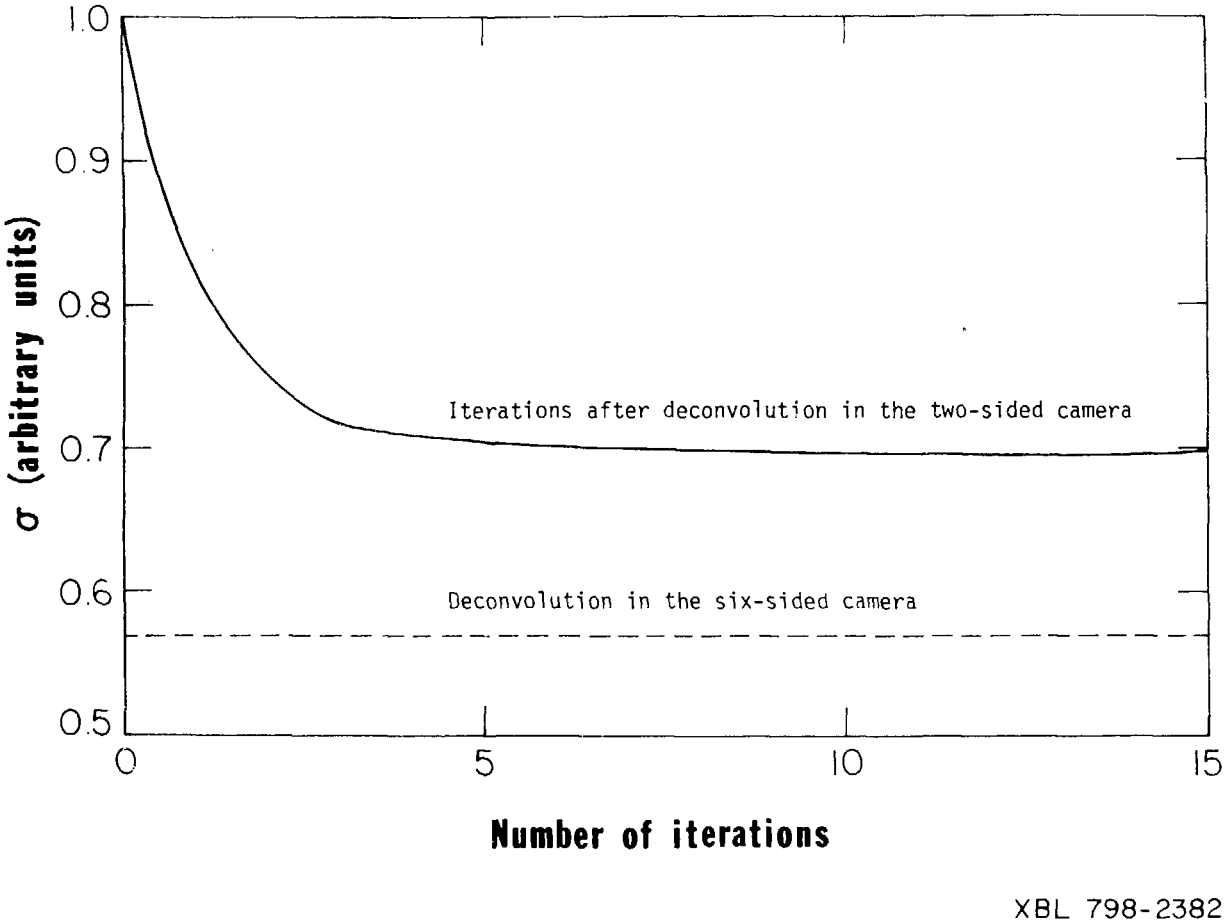

XBL 798-2382

Fig. 4.19. The values of the root mean square deviation of the deconvolved image in the two-sided camera as a function of the number of iterations.

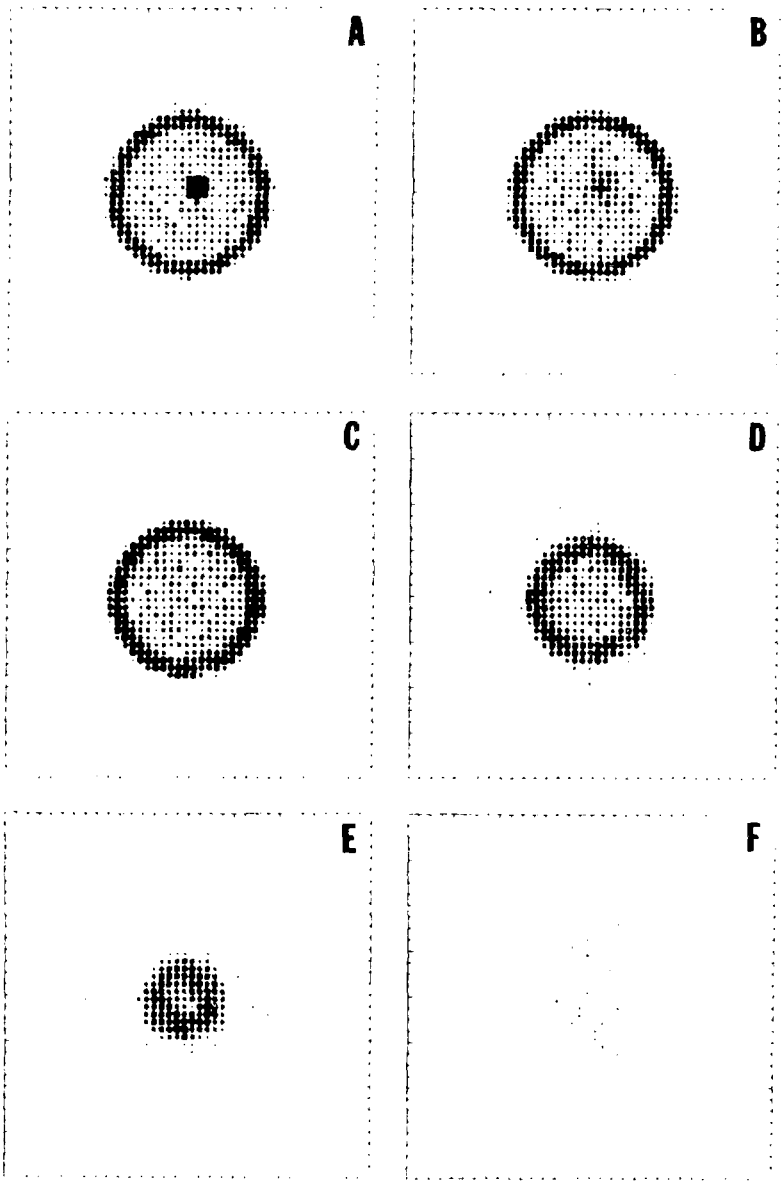

XBL 797-10703

Fig. 4.20. The deconvolved image in Fig. 4.11 after 10 iterations using the scheme shown in Fig. 2.21.

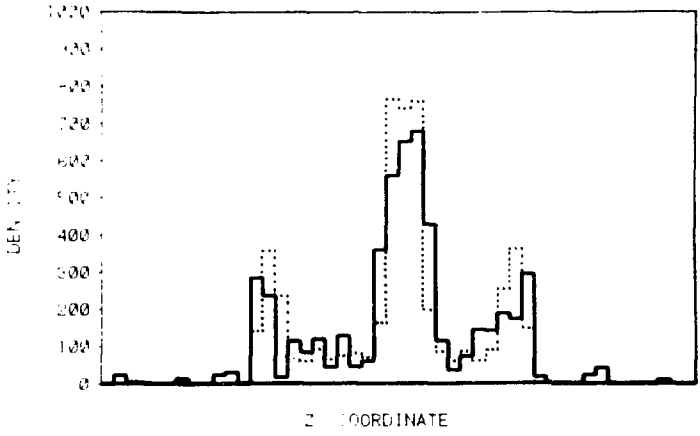

XBL 7910-12144

Fig. 4.21. Profile of the image in Fig. 4.20 along the line i = j = 25.

Fig. 4.22. Back-projection image of a real phantom which consists of a cylindrical shell to simulate a skull, and 2 cylindrical tumors. The shell is 1.5 cm thick, 16.5 cm high, and has an inner radius of 7.5 cm. Each tumor is 4 cm high and has a radius of 1 cm. The concentration ratio is 5:1 for the skull and one tumor, and 10:1 for the other. Each picture element is 0.5×0.5 cm^2. The planes are 2 cm apart in the z direction.

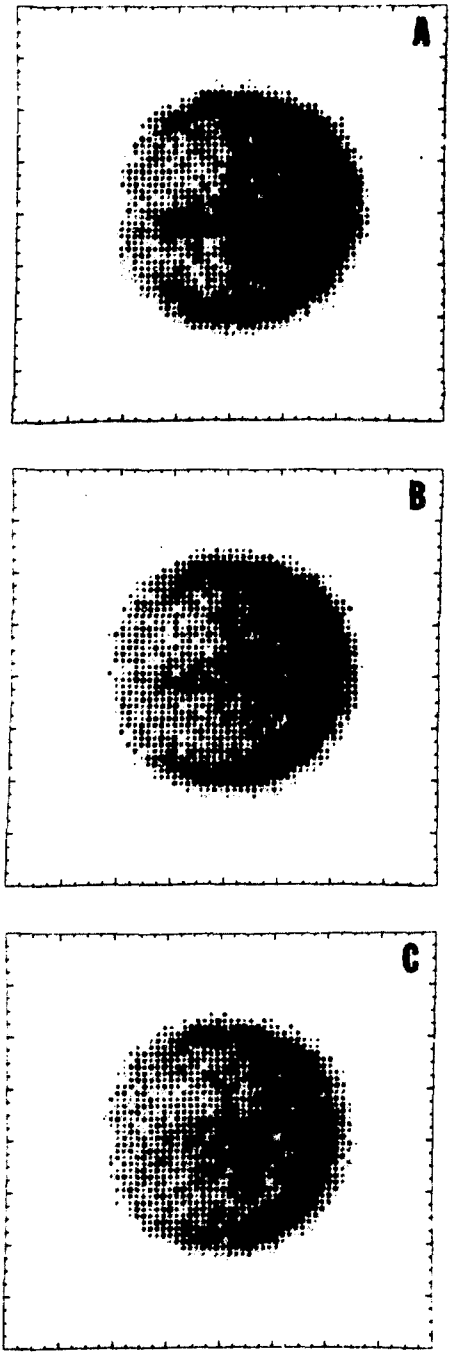

Fig. 4.23. Back-projection of the data from the real phantom with 55% background subtraction.

XBB 799-11797

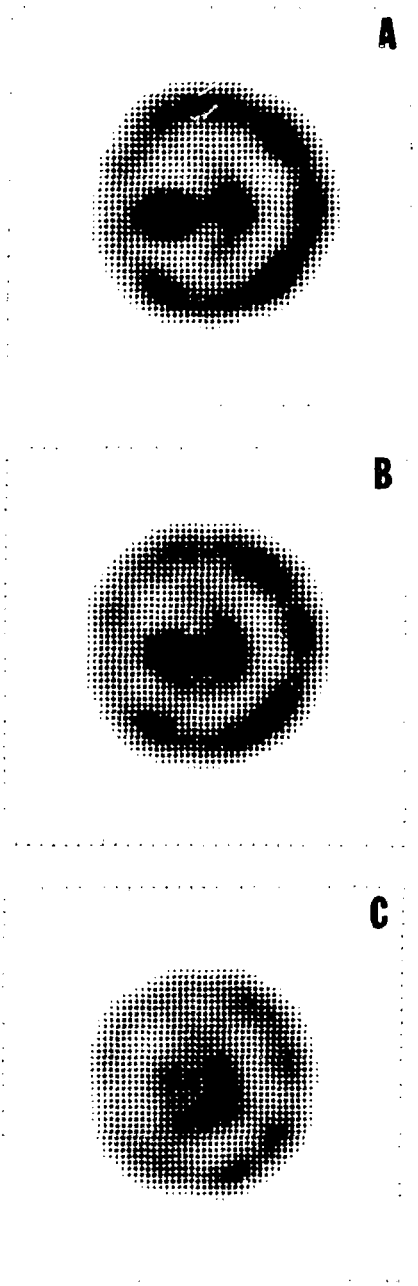

Fig. 4.24. Reconstruction of the real phantom by Fourier deconvolution + 4 iterations.
Angular factor: $F(\theta) = \cos^{-12}\theta$.
Filtering parameters: $m = 10$, $\gamma = 35.9$.
XBB 799-11800

V. DISCUSSIONS AND CONCLUSIONS

5.1. Discussions

Compared to cameras using detectors such as NaI, the present MWPC-Pb converter position camera has excellent spatial resolution and the advantage of low cost, but suffers in the area of inadequate detection efficiency. Roughly speaking, the conversion efficiency of the gamma converter is determined by the total amount of surface area available for interacting with the gammas, and thus can be increased either by decreasing the cell size of the converter, as illustrated in Fig. 2.6, or by increasing its height. Both decrease in cell size and increase in height are made possible through the use of PbO-glass converter [53].

Due to its more uniform electric drift field, the drift time spread in electron collection T_c in a PbO-glass converter is much shorter than in a Pb converter, being 110 nsec for a 15 mm high PbO-glass converter compared to 330 nsec for a Pb converter of the same hieght. The reduction in T_c makes it possible to use converters of increased height. The increased uniformity of the drift field also means higher extraction efficiency ε_e, as implied in Fig. 2.9, and thus converters with smaller cell size can be used. Fabrication of PbO-glass converters with cell size $\sim$ 1 mm is readily achievable by fusing together PbO-glass tubings followed by slicing. Recent measurements on a PbO-glass converter of cell size 1.4 mm and height 2 cm yielded 8% detection efficiency [54]. This translates into a nine-fold increase in the coincidence count rate over the present camera system equipped with Pb converters.

limitation on the minimum size of the angle of the allowed cone that can be used in limited-angle imaging. The minimum practical allowed-cone angle is primarily governed by the accuracy of the digital computer employed for computation, which sets a limit on the minimum magnitude of the eigenvalues that can be computed, and hence determines the number of eigenfunction components of the object that can be recovered in the iterations.

One way to improve on the situation is to use direct inversion to solve for the missing-cone frequency components instead of using iterations. Sabri and Steenaart developed the extrapolation matrix [56] for such a purpose. This approach requires inverting a matrix of order $m \times m$, where m is the number of frequency components in the allowed cone and missing cone combined. As m usually ranges from a few thousand upwards in two-dimensional and even more in three-dimensional imaging, extrapolation matrix is not very practical in such applications.

Another approach is to devise schemes to accelerate the iterations, possibly through the use of other constaints on the object or its Fourier components, such as boundedness in object density, continuity, etc, Positivity [57, 58] has already been utilized in our iterations: all the negative values in the object density were set to zero after each Fourier transform. This procedure produced a 20% reduction in σ for the 2-D point sources in Figs. 4.8 - 4.9. For ordinary phantoms with extended regions of positive density, the reduction in σ was much smaller, about 0.5%, due to swamping of most of the negative-undershoot artifact of each point source by the positive density values of other point sources.

APPENDIX A

EVALUATION OF $I = \int_0^{t/2} (L + 2x)\, P_{esc}(x, E_i)dx$

We consider the following 2 cases:

Case 1 $R(E_i) < t/2$

$t - x > 2R(E_i) - x \cdot R(E_i)$

$\therefore P(t - x, E_i) = 0.$

In this case we only have to evaluate

$$\int_0^{t/2} (L + 2x)\, P(x, E_i)dx$$

$$= \int_0^{R(E_i)} (L + 2x)\, P(x, E_i)dx.$$

Putting $y = \frac{1}{1 - \frac{x}{R(E_i)}}$ and integrating we get

$$I = \frac{R(E_i)}{A^2}\,[2R(E_i) + L(A + 1)].$$

Case 2 $R(E_i) \geq t/2$

$$I = \int_0^{t/2} (L + 2x)\, P_{esc}(x, E_i)$$

$$= \int_0^{t/2} (L + 2x)\, P(x, E_i)dx + \int_0^{t/2} (L + 2x)\, P(t - x, E_i)dx.$$

Changing variables and collecting terms, we have

$$I = L \int_0^t P(x, E_1)dx + 2\left\{ \int_0^{t/2} x\ P(x, E_i)dx - \int_{t/2}^t x\ P(x, E_1)dx \right\}$$

$$+ 2t \int_{t/2}^t P(x, E_1)dx$$

$$= I_1 + I_2 + I_3$$

$$I_1 = L \int_0^t P(x, E_1)dx$$

$$= L \exp(A) \int_0^t \exp\left(\frac{-A}{1 - \frac{x}{R(E_1)}} \right) \left(1 - \frac{x}{R(E_1)} \right)^{-3} dx$$

$$= \frac{L\, R(E_1)\, \exp(A)}{A} \left(f(1) - \begin{cases} f(y_{t,1}) & \text{if } t < R(E_1) \\ f(0) & \text{if } t > R(E_1) \end{cases} \right)$$

where

$$f(y) = \exp(-Ay)(y + \frac{1}{A}),\ y_{t,1} = \left(1 - \frac{t}{R(E_1)} \right)^{-1}.$$

To find I_2, we first evaluate the integral

$$\int x\ P(x, E_1)dx$$

$$= \exp(A) \int x \exp\left(\frac{-A}{1 - \frac{x}{R(E_1)}} \right) \left(1 - \frac{x}{R(E_1)} \right)^{-3} dx.$$

Putting $y = \left(1 - \frac{x}{R(E_1)} \right)^{-1}$, we get

$$\int x\ P(x, E_1)dx = \frac{\exp(A)\ R(E_1)^2}{A} \exp(-Ay)(1 - y - \frac{1}{A}).$$

Substituting into I_2 we obtain

$$I_2 = \frac{2\exp(A)R^2(E_i)}{A}\left(2g(y_{t/2,i}) - g(1) - \begin{cases} g(y_{t,i}) & \text{if } t \le R(E_i) \\ 0 & \text{if } t > R(E_i) \end{cases}\right)$$

where

$$g(y) = \exp(-Ay)\,(1 - y - \frac{1}{A}).$$

Similarly we have

$$I_3 = \frac{2t}{A}\left(f(y_{t/2,i}) - \begin{cases} f(y_{t,i}) & \text{if } t \le R(E_i) \\ 0 & \text{if } t > R(E_i). \end{cases}\right)$$

The results are summarized as follows:

$$t \le R(E_i),\quad I = \frac{\exp(A)\,R(E_i)}{A}\Big\{L[f(1) - f(y_{t,i})] + 2R(E_i)[2g(y_{t/2,i}) - g(y_{t,i}) - g(1)] + 2t[f(y_{t/2,i}) - f(y_{t,i})]\Big\}$$

$$R(E_i) < t \le 2R(E_i),\quad I = \frac{\exp(A)R(E_i)}{A}\Big\{Lf(1) + 2R(E_i)[2g(y_{t/2,i}) - g(1)] + 2t\,f(y_{t/2,i})\Big\}$$

$$2R(E_i) < t,\quad I = \frac{R(E_i)}{A^2}\,[2R(E_i) + L\,(A+1)].$$

APPENDIX B

TRACK-LENGTH DISTRIBUTION INSIDE AN INFINITELY LONG CYLINDER WITH SOURCE POINT OUTSIDE THE CYLINDER

Consider the family of lines generated from the source point (located at the origin) and intersecting the cylinder (see Fig. B.1). Let the line characterized by the polar angle and the azimuth (θ, ϕ) intersect the surface of the cylinder at distances R_1 and R_2 from the source point. R_1 and R_2 both satisfy the equation

$$(R \sin\theta \cos\phi)^2 + (R \sin\theta \sin\phi - b)^2 = a^2 .$$

Solving the quadratic equation gives

$$R_{1,2} = \frac{2b \sin\theta \sin\phi \pm \sqrt{4b^2 \sin^2\theta \sin^2\phi - 4 \sin^2\theta (b^2 - a^2)}}{2 \sin^2\theta} .$$

The track length inside the cylinder ΔR is

$$\Delta R = |R_1 - R_2| = \frac{2\sqrt{b^2 \sin^2\phi - (b^2 - a^2)}}{|\sin\theta|}$$

$$\frac{\Delta R}{2a} = \frac{\sqrt{(\frac{b}{a})^2 \sin^2\phi - ((\frac{b}{a})^2 - 1)}}{|\sin\theta|} .$$

Define $r = \frac{\Delta R}{2a}$, $c = \frac{b}{a}$, $x = \cos\theta$. The above expression then becomes

$$r = \frac{\sqrt{c^2 \sin^2\phi - (c^2 - 1)}}{\sqrt{1 - x^2}} .$$

Due to the symmetry of the geometry, the domains of ϕ and x can be taken to be $(\phi_0, \pi/2)$ and $(0,1)$ respectively, where $\phi_0 = \sin^{-1} \frac{\sqrt{c^2 - 1}}{c}$.

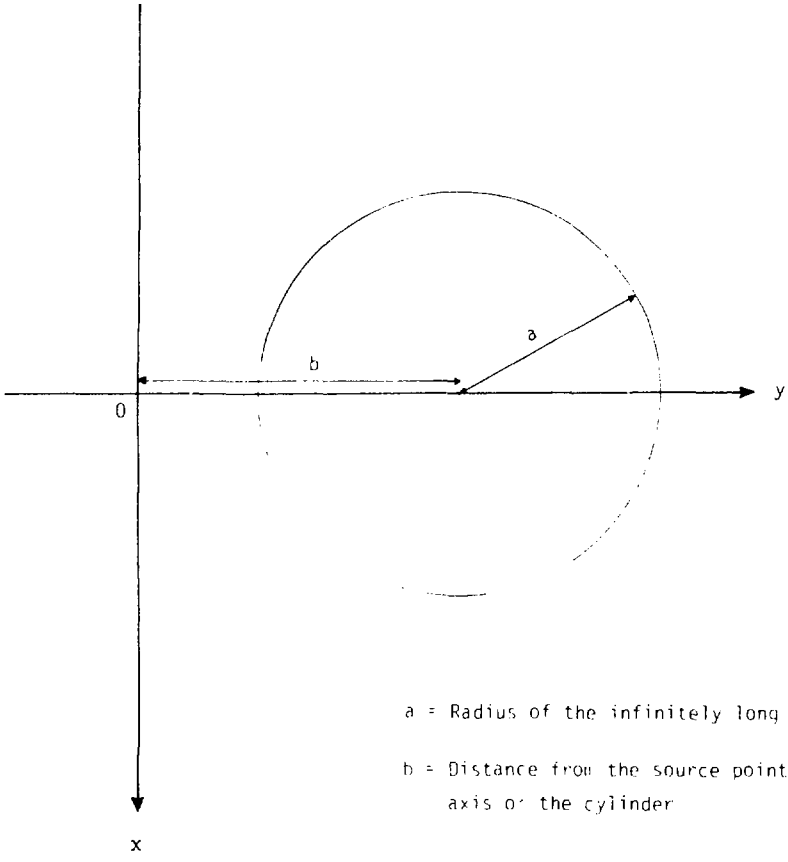

Fig. B.1. Geometry for calculating the track-length distribution inside an infinitely long cylinder.

The distribution of (r, w) is obtained from (B.1), (B.2) and (B.6):

$$f_{rw}(r, w) = \frac{f_{\phi, x}(\phi, x)}{J\left(\frac{r, w}{\phi, x}\right)}$$

$$= \frac{f_{\phi}(\phi)\ f_{x}(x)}{J\left(\frac{r, w}{\phi, x}\right)}$$

$$= \frac{2r}{\pi} \frac{(1 - w^2)}{\sqrt{r^2(1-w^2) + (c^2-1)}\sqrt{1 - r^2(1-w^2)}}.$$

The track-length distribution is thus given by

$$f(r) = \frac{2r}{\pi} \int_0^1 \frac{(1 - w^2)dw}{\sqrt{r^2(1-w^2) + (c^2-1)}\sqrt{1 - r^2(1-w^2)}}.$$

Case 2: $r > 1$

In this case we put

$$r = \frac{\sqrt{c^2 \sin^2\phi - (c^2-1)}}{\sqrt{1 - x^2}}$$

$$w = \phi.$$

Following exactly the same procedure used in case 1, we get

$$f(r) = \frac{2}{\pi r^3} \int_{\phi_0}^{\pi/2} \frac{c^2 \sin^2 w - (c^2-1)}{\sqrt{1 - \frac{c^2 \sin^2 w - (c^2-1)}{r^2}}} dw.$$

APPENDIX C.

DERIVATION OF THE FACTOR $C(T_r/T_c)$ IN THE TRUE COINCIDENCE RATE WHEN $T_r \leq T_c$.

If $T_r \leq T_c$, true coincidence rate and hence the ratio of true to chance coincidences as given by equations (2.2) and (2.4) are modified by a factor $C(T_r/T_c)$, which is the probability that the two elections e_1 and e_2 generated in detector A and detector B respectively in an annihilation event will be in coincidence within the time T_r. Referring to Fig. C.1, this quantity is given by

$$\begin{aligned} C(T_r/T_c) &= \text{probability that } | t_1 - t_2 | \leq T_r \\ &= P\left\{ | t_1 - t_2 | \leq T_r \right\}. \end{aligned}$$

We consider the following two cases:

Case 1. $T_r < T_c/2$

Partition the time interval T_c for detector A into the 3 intervals I, II and III, as shown in Fig. C.2.

If e_1 occurs within the interval I,

$$P\left\{ e_1 \text{ occurring within } dt_1 \text{ at } t_1 \right\} = \frac{dt_1}{T_r}$$

$$P\left\{ |t_1 - t_2| \leq T_r \middle| e_1 \text{ occurring within } dt_1 \text{ at } t_1 \right\} = \frac{t_1 + T_r}{T_c},$$

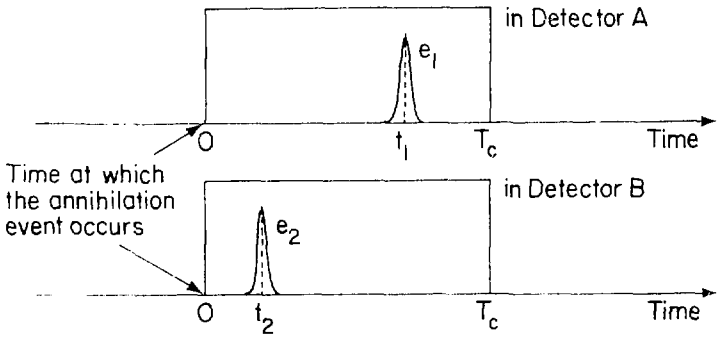

Fig. C.1. Occurrence of detected signals.

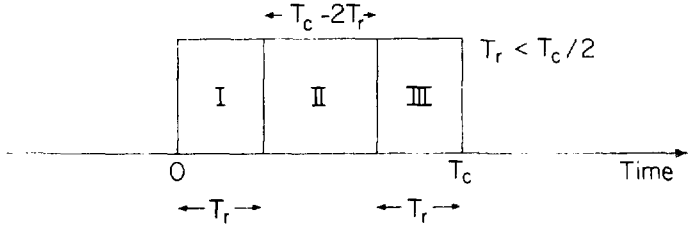

Fig. C.2. Partition for $T_r < T_c/2$.

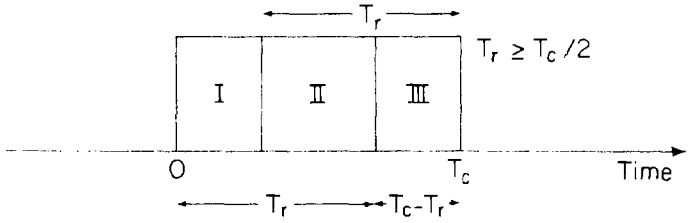

XBL 798-2386

Fig. C.3. Partition for $T_r \geq T_c/2$.

Case 2. $T_r \geq T_c/2$

Partition the time interval T_c for detector A into the 3 intervals I, II and III, as shown in Fig. C.3. Similar to case 1, we have

$$C_I\ (T_r/T_c) = C_{III}\ (T_r/T_c) = \frac{3}{2}\ \frac{T_r}{T_c}\ .$$

For the interval II,

$$C_{II}\ (T_r/T_c) = 1\ .$$

Combining the contributions from I, II, and III we have

$$C\ (T_r/T_c) = \frac{T_c - T_r}{T_c}\ \frac{3\ T_r}{2\ T_c} + \frac{2\ T_r - T_c}{T_c} + \frac{T_c - T_r}{T_c}\ \frac{3\ T_r}{T_c}$$

$$= 2\ (T_r/T_c) - (T_r/T_c)^2\ .$$

APPENDIX D

EVALUATION OF THE TWO-DIMENSIONAL OPTICAL TRANSFER FUNCTION

$$\begin{aligned}\Phi_0(k_x,k_z) &= \int_{-\infty}^{\infty} dz \int_{-\infty}^{\infty} dx\ \phi_0(x,z)\ \exp(2\pi i(k_x x + k_z z)) \\ &= \int_{-\infty}^{\infty} dz \int_{-\pi}^{\pi} d\theta\ \phi_0(\theta,z) \exp(2\pi i z(k_x \tan\theta + k_z))\,|z|\sec^2\theta \\ &= \int_{-\theta_0}^{\theta_0} d\theta\ \frac{F(\theta)}{\pi} \int_{-\infty}^{\infty} dz\ \exp(2\pi i z(k_x \tan\theta + k_z)).\end{aligned}$$

Now

$$\int_{-\infty}^{\infty} \exp(2\pi i z(k_x \tan\theta + k_z))dz = \delta(k_x \tan\theta + k_z) \qquad (D.1)$$

therefore

$$\Phi_0(k_x,k_z) = \int_{-\theta_0}^{\theta_0} \frac{F(\theta)}{\pi}\ \delta(k_x \tan\theta + k_z)d\theta$$

$$= \begin{cases} \dfrac{\delta(k_z)}{\pi} \displaystyle\int_{-\theta_0}^{\theta_0} F(\theta)d\theta & \text{if } k_x = 0 \\ \dfrac{F(\theta_i)\cos^2\theta_i}{\pi|k_x|} & \text{if } k_x \neq 0 \end{cases} \qquad (D.2)$$

where $\tan\theta_i = -\dfrac{k_z}{k_x}$.

APPENDIX E

EVALUATION OF THE THREE-DIMENSIONAL OPTICAL TRANSFER FUNCTION

In three dimensions, equation (2.9) takes the form

$$\phi_0(\underline{s}, z)|z|^2 = H(\underline{s}/z) \tag{E.1}$$

where $\underline{s} = (x,y)$, and the angular function H is positive inside the data cone and zero outside. Defining $\underline{t} = \underline{s}/z$, $\underline{w} = (k_x,k_y)$, and performing the Fourier transformation, we get

$$\begin{aligned}\Phi_0(\underline{w},k_z) &= \int dz \iint d^2 \phi_0(\underline{s},z) \exp(2\pi i(\underline{w}\cdot\underline{s} + k_z z)) \\ &= \iint H(\underline{t})\, \delta(\underline{w}\cdot\underline{t} + k_z) d^2t .\end{aligned}$$

The vector $\underline{t} = (t_1,t_2)$ can be chosen so that t_1 lies along $\underline{w}$, giving $\underline{w}\cdot\underline{t} + k_z = |\underline{w}|\, t_1 + k_z$. Then we get

$$\Phi_0(\underline{w},k_z) = \begin{cases} \delta(k_z) \iint H(\underline{t}) d^2t & \text{if } \underline{w} = 0 \\ \int H(-k_z/|\underline{w}|,\ t_2) dt_2 & \text{if } \underline{w} \neq 0 . \end{cases} \tag{E.2}$$

In the particular case where ϕ_0 is in form of a square pyramid, i.e.,

$$\begin{aligned}\phi_0(x,y,z) > 0 \text{ whenever } &0 \leq |x| \leq |z\tan\theta_0| \\ &\text{and } 0 \leq |y| \leq |z\tan\theta_0|\end{aligned}$$

application of (E.2) shows that

$$\begin{aligned}\Phi_0(k_x,k_y,k_z) > 0 \text{ if } &(|k_x| + |k_y|) > |k_z|/\tan\theta_0 \text{ when } |k_x|,\ |k_y| > 0 \\ &\text{or } (|k_x| + |k_y|) \geq |k_z|/\tan\theta_0 \text{ when } |k_x| = 0 \text{ or } |k_y| = 0\end{aligned} \tag{E.3}$$

$$= 0 \text{ otherwise .}$$

APPENDIX F

NECESSARY AND SUFFICIENT CONDITION FOR AN OPTICAL TRANSFER FUNCTION TO BE NON-ZERO EVERYWHERE

In this Appendix we prove the statement (2.11), namely, the necessary and sufficient condition for an optical transfer function to be non-zero everywhere is that every plane passing through the origin of the corresponding point response function contain at least a line of non-zero values.

Necessity

If there is a plane A through the origin of Φ_0 on which only the origin is non-zero, then we take the normal to A at the origin to be the z-axis. Equation (E.2) shows that Φ_0 is zero on the k_z-axis except at the origin.

Sufficiency

Given a point response function satisfying condition (2.11), we want to show that the value of Φ_0 at any arbitrary point P in the frequency space is non-zero. First rotate the coordinate system in frequency space so that P lies on the k_x-axis. The plane $x = 0$ contains at least one line on which Φ_0 is non-zero. Take any such line to be the z-axis. Then decompose Φ_0 into two parts in the following manner:

$$\phi_0^{(1)}(x, y, z) = \begin{cases} 0 & \text{if } z = 0 \\ \phi_0(x, y, z) & \text{if } z \neq 0 \end{cases}$$

$$\phi_0^{(2)}(x, y, z) + \begin{cases} \phi_0(x, y, z) & \text{if } z = 0 \\ 0 & \text{if } z \neq 0. \end{cases}$$

Clearly $\phi_0 = \phi_0^{(1)} + \phi_0^{(2)}$. Since $\phi_0^{(1)}$ satisfies (E.1), equation (E.2) shows that $\phi_0^{(1)} > 0$, because $H(\underline{t}) > 0$ at $\underline{t} = 0$. Now it remains to show that $\phi_0^{(2)}$ is non-negative at P. $\phi_0^{(2)}$ can be written as

$$\phi_0^{(2)}(s, \theta, z) = \frac{F(\theta)\ \delta(z)}{s}$$

where we have made the coordinate transformation $r(x, y) \rightarrow r(s, \theta)$. Transforming $k(k_x, k_y)$ to polar coordinate $k(w, \alpha)$, and taking the Fourier transform of $\phi_0^{(2)}$, we get

$$\phi_0^{(2)}(w, \alpha, k_z) = \iiint \frac{F(\theta)\ \delta(z)}{s} \exp(2\pi i (sw\cos(\theta-\alpha) + k_z z)) s\,ds\,d\theta\,dz$$

$$= \frac{F(\alpha + \pi/2)}{2\pi |w|}$$

which is clearly non-negative.

APPENDIX G

EFFECTS OF SAMPLING $\phi_0(x, z)$ IN THE x AND z DIMENSIONS.

Let the object distribution $\rho(\underline{r})$ be sampled in the z dimension by the sampling function:

$$s_{\Delta z}(z) = \sum_{n=-\infty}^{\infty} \delta(z - n\Delta z).$$

The point response function $\phi_0(x, z)$ can thus be sampled in the same way. By the convolution theorem, the optical transfer function $\Phi_0^{(z)}(k_x, k_z)$ of the sampled $\phi_0(x, z)$ is given by

$$\Phi_0^{(z)}(k_x, k_z) = \Phi_0(k_x, k_z) * S_{\Delta k_z}(k_z) \qquad (G.1)$$

where $\Phi_0(k_x, k_z)$ is the original optional transfer function, $S_{\Delta k_z}(k_z)$ is the Fourier transform of $s_{\Delta z}(z)$, and * denotes convolution. Now reference [63] shows that $S_{\Delta k_z}(k_z)$ is also a sampling function in the k_z dimension given by

$$S_{\Delta k_z}(k_z) = \Delta k_z \sum_{n=-\infty}^{\infty} \delta(k_z - n\Delta k_z), \quad \Delta k_z = \frac{1}{z_2 - z_1}. \qquad (G.2)$$

From equations (G.1) and (G.2) we see that $\Phi_0^{(z)}(k_x, k_z)$ is the superimposition of repetitions of the original optical transfer function in the k_z dimension at intervals of Δk_z. Thus $\Phi_0^{(z)}(k_x, k_z)$ is non-zero in the region $2|k_x| \tan\theta_0 \geq \Delta k_z$; as for the region $2|k_x| \tan\theta_0 < \Delta k_z$,

the number of zero Fourier components is reduced by a factor of 2.

If sampling of $\phi_0(x, z)$ is done in the x dimension instead, similar considerations show that the corresponding optical transfer function $t_0^{(x)}(k_x, k_z)$ will be non-zero everywhere.

By well known theorem in variational calculus, the lower bound of this ratio for all z-limited functions is equal to the infimum α_{min} of the eigenvalues $\{\alpha_i\}$ of the integral operator.

$$\alpha_i g_i(z) = \int_{z_1}^{z_2} \left(\int_{-s_0}^{s_0} \frac{G(s)}{k_x \pi} \exp(-2\pi i s(z-z')) ds \right) g_i(z') dz'.$$

We want to prove that $\alpha_{min} = 0$. Assume $\alpha_{min} > 0$. Let G_0 be the maximum value of $\frac{G(s)}{k_x \pi}$ in $(-s_0, s_0)$. For the special case $\frac{G(s)}{k_x \pi} = 1$, the eigenvalues λ_i of the integral equation

$$\lambda_i f_i(z) = \int_{z_1}^{z_2} \left(\int_{-s_0}^{s_0} \exp(-2\pi i s(z-z')) ds \right) f_i(z') dz'$$

go to zero as the index $i \to \infty$ [35], so there is an integer m such that $G_0 \lambda_m < \alpha_{min}$. Substituting the z-limited function $f_m(z)$ and its Fourier transform $F_m(s)$ into the expression (I.2) we get

$$0 < \frac{\int_{-s_0}^{s_0} |F_m(s)|^2 \frac{G(s)}{k_x \pi}}{\int_{-\infty}^{\infty} |F_m(s)|^2 ds} \leq \frac{G_0 \int_{-s_0}^{s_0} |F_m(s)|^2 ds}{\int_{-\infty}^{\infty} |F_m(s)|^2 ds}$$

$$= \lambda_m G_0 < \alpha_{min}$$

which contradicts the definition of α_{min}. Thus α_{min} is equal to zero.

[13] Lim, C.B., Chu, D., Kaufman, L., Perez-Mendez, V., Hattner, R., and Price, D. C., IEEE Trans. Nucl. Sci., NS-22 (1975) 388.

[14] Heitler, W., 1944, Quantum Theory of Radiation (London: Oxford University Press) p. 230 ff.

[15] Ore, A., Powell, J. L., Phys. Rev., 75 (1949)1697.

[16] DeBenedetti, S., Cowan, C. E., Konneker, W. R., and Primakoff, H., Phys. Rev., 77 (1950) 205.

[17] Charpak, G., Bouclier, R., Bressani, T., Favier, J., and Zupancic, C., Nucl. Instr. and Meth., 62 (1968) 262.

[18] Kaufman, L., Perez-Mendez, V., Shames, D., and Stoker, G., IEEE Trans. Nucl. Sci., NS-19 (1972) 169.

[19] Erskine, G. A., CERN report, Nucl. Instr. and Meth.,105 (1972) 565.

[20] Rose, M. E., and Korff, S. A., Phys. Rev., 59 (1941) 850.

[21] Bleaney, B. J., and Bleaney, B., 1965, Electricity and Magnetism (London:Oxford University Press) p. 304.

[22] Grove, R., Ko, I., Leskovar, B., Perez-Mendez, V., Nucl. Instr. and Meth., 99 (1972) 381.

[23] Bradt, H., Helv. Phys. Acta., 19 (1946) 77.

[24] Lim, C. B., Chu, D., Kaufman, L., Perez-Mendez, V., and Sperinde, J., IEEE Trans. Nucl. Sci., NS-21 (1975) 85.

[25] Jeavons, A. P., Charpak, G., Stubbs, R. J., IEEE Trans. Nucl. Sci., NS-22 (1975) 297.

[26] Spencer, L. V., Phys. Rev., 98 (1955) 1597.

[27] Seliger, H. H., Phys. Rev., 88 (1952) 408.

[28] Morse, P. M., and Feshbach, H., 1953, Methods of Theoretical Physics (New York: McGraw-Hill) Part I: chapter 8.

[29] Chang, L. T., Macdonald, B., and Perez-Mendez, V., IEEE Trans. Nucl. Sci., NS-23 (1976) 568.

[30] Riesz, F., and Sz.-Nagy, B., 1955, Functional Analysis (New York: Frederick Ungar) chapter 6.

[31] Harris, J. L., J. Opt. Soc. Am., 54 (1964) 931-936.

[32] Whittaker, E. T., and Watson, G. N., 1952, A Course of Modern Analysis (England: Cambridge University Press) p. 67.

[33] Solomon, D. C., J. Math. Anal. Appl., 56 (1976) 61-83.

[34] Smith, K. T., Solmon, D. C., and Wagner, S. L., Bull. Amer. Math. Soc., 83 (1977) 1227-1270.

[35] Slepian, D., and Pollak, H. O., Bell Syst. Tech. J., 40 (1961) 43.

[36] Barnes, C. W., J. Opt. Soc. Am., 56 (1966) 575.

[37] Inouye, T., IEEE Trans. Nucl. Sci., NS-26 (1979) 2666.

[38] Gerchberg, R. W., Optica Acta, 21 (1974) 709-720.

[39] Papoulis, A., IEEE Trans. Circuits Syst., CAS-22 (1975) 735-742.

[40] Slepian, D., Bell Syst. Tech. J., 43 (1964) 3009.

[41] Bateman, J. E., Nucl. Instr. and Meth., 140 (1977) 211.

[42] Phillips, D. L., J. Ass. Comp. Mach., 9 (1962) 84.

[43] Slepian, D., and Sonnenblick, E., Bell Syst. Tech. J., 44 (1965) 1745.

[44] Twomey, S., J. Ass. Comp. Mach., 10 (1963) 97.

[45] Grove, R., Perez-Mendez, V., Sperinde, J., Nucl. Instr. and Meth., 106 (1973) 407.

[46] Chu, D., Ph.D Thesis, University of California, Berkeley, Calif. (1976).

[47] Radeka, V., IEEE Trans. Nucl. Sci., NS-21 (1973) 51.

[48] Bhandari, N., Perez-Mendez, V., and Kirsten, F., LBL-report (1976).

[49] Perez-Mendez, V., Greenstein, M., and Ortendahl, D., IEEE Trans. Nucl. Sci., NS-24 (1977) 209.

[50] Brigham, E. O., 1974, The Fast Fourier Transform (Englewood Cliffs, N. J. : Prentice Hall).

[51] Blackman, R. B., and Tukey, J. W., 1958, The Measurement of Power Spectra from the Point of View of Communications Engineering (New York: Dover) p. 98.

[52] Singleton, R. C., IEEE Trans. Audio and Electroacoustics, AU-17 (1969) 93.

[53] Chu, D., Tam, K. C., Perez-Mendez, V., Lim, C. B., Lambert, D., Kaplan, S. N., IEEE Trans. Nucl. Sci., NS-23 (1976) 634.

[54] Lum, G. K., Green, M. I., Perez-Mendez, V., and Tam, K. C., IEEE Trans. Nucl. Sci., to be published.

[55] Crowther, R. A., DeRosier, D. J., and Klug, A., Proc. Roy. Soc. Lond. A, 317 (1970) 319-340.

[56] Sabri, M. S., and Steenaart, W., IEEE Trans. Circuits Syst., CAS-25 (1978) 74.

[57] Frieden, B. R., J. Opt. Soc. Am., 62 (1972) 511.

[58] Frieden, B. R., and Burke, J. J., J. Opt. Soc. Am., 62 (1972) 1202.

[59] Brenner, N. M., IEEE Trans. Audio and Electroacoustics, AU-17 (1969) 128.

[60] Buijs, H. L., Applied Optics, 8 (1969) 211.

[61] Singleton, R. C., IEEE Trans. Audio and Electroacoustics, AU-15 (1967) 91.

[62] Papoulis, A., 1965, Probability, Random Variables, and Stochastic Process (New York: McGraw-Hill) p. 201.

[63] Papoulis, A., 1962, The Fourier Integral and Its Applications (New York: McGraw-Hill) p.44.